Faraday wave–droplet dynamics: discrete-time analysis

Matthew Durey[1],[†] **and Paul A. Milewski**[1]

[1]Department of Mathematical Sciences, University of Bath, Bath BA2 7AY, UK

A droplet may 'walk' across the surface of a vertically vibrating bath of the same fluid, due to the propulsive interaction with its wave field. This hydrodynamic pilot-wave system exhibits many dynamics previously believed to exist only in the quantum realm. Starting from first principles, we derive a discrete-time fluid model, whereby the bath–droplet interactions are modelled as instantaneous. By analysing the stability of the fixed points of the system, we explain the dynamics of a walking droplet and capture the quantisations for multiple-droplet interactions. Circular orbits in a harmonic potential are studied, and a double quantisation of chaotic trajectories is obtained through systematic statistical analysis.

Key words: bifurcations, drops, Faraday waves

1. Introduction

Faraday waves and droplet impact have been separate research areas for much of the last century. Although Walker ([1978](#)) showed that a droplet may 'float' on a vertically vibrating bath of fluid, it was not until the last decade that this connection was re-explored. In 2005, Couder and co-workers showed that for sufficiently large, yet subcritical, vibrations of the liquid bath, a droplet may bounce periodically on the surface (Couder *et al.* [2005*b*](#)). At each impact, a capillary wave propagates away from the droplet, exciting a field of standing Faraday waves in its wake. For larger forcing, the bouncing destabilises, and the droplet 'walks' across the surface of the bath, propelled at each impact by the slope of its associated wave field. As the forcing vibration increases, so does the decay time of the Faraday waves. This yields a path 'memory' from previous droplet impacts (Eddi *et al.* [2011](#)), leading to a macroscopic particle–wave interaction, as previously envisaged as an explanation for quantum behaviour (de Broglie [1926](#)). This analogy has since been explored through a remarkable series of experiments, summarised in detail by Bush ([2015](#)).

Several quantum analogies have been pursued. A walking droplet passing through a slit between submerged walls yielded the diffraction and interference patterns for single- and double-slit experiments respectively (Couder & Fort [2006](#), [2011](#)). This effect was due to the interaction of the wave field with the walls. Furthermore, a droplet may 'tunnel' across the submerged wall separating two deep regions; as the wall width increases, the tunnelling probability decreases (Eddi *et al.* [2009](#)). Moreover,

† Email address for correspondence: m.durey@bath.ac.uk

Harris *et al.* (2013) found that the position of a chaotic walker in a circular corral exhibits wave-like statistics, whose maxima correspond to the zeros of the fundamental Faraday mode. This is reminiscent of an electron in a quantum corral.

The interaction between droplets also yields quantum analogues, such as fixed lattices of bouncing droplets and bound states (Protière, Boudaoud & Couder 2006; Eddi *et al.* 2008). At the approach of two walking droplets, the interaction between wave fields leads to either scatter or locking in circular orbital motion with quantised orbit diameters (Couder *et al.* 2005b). For droplets of different sizes, one droplet may orbit the other, with complex epicycles emerging (Protière, Bohn & Couder 2008). Two droplets walking in parallel interact through the wave field, and stable transverse oscillations ensue (Protière *et al.* 2006); these 'promenade' modes have been observed to have quantised average distances between the droplets (Borghesi *et al.* 2014).

Further analogues occur when a droplet walks on a rotating bath. Due to the Coriolis force, the droplet moves in a circular motion in the rotating frame (Fort *et al.* 2010). As the forcing vibration is increased, the wave field forces the orbit diameters to be quantised, with a macroscopic analogy to Landau levels (Oza *et al.* 2014a). In the long-memory limit, more exotic trajectories occur, including drifting, wobbling and quasi-periodic orbits (Oza *et al.* 2014b). In particular, the stationary probability distribution for the droplet position exhibits wave-like statistics, with maxima at its unstable steady states (Harris & Bush 2014). Two droplets may orbit each other in the rotating frame, but their orbit diameters exhibit Zeeman-like splitting depending on whether the orbits are co-/anti-rotational relative to the bath (Eddi *et al.* 2012).

Circular orbits also exist for a droplet in a harmonic potential (Perrard *et al.* 2014b), with their convergence explored by Labousse & Perrard (2014). At long memory, the orbit diameters are quantised (Labousse *et al.* 2016), and an array of stable exotic trajectories forms, with a double quantisation in their average radius and angular momentum (Perrard *et al.* 2014b). The underlying pivot structure of the wave field governing these trajectories has been explored by Labousse *et al.* (2014). In the chaotic regime, the switching time between trajectories is probabilistic (Perrard *et al.* 2014a).

The above dynamics are governed by a complex set of physical phenomena. For a bath vibrated sinusoidally with amplitude A and frequency $\omega_0/(2\pi)$, the stability of the Faraday waves is governed by $\Gamma = A\omega_0^2/g$, which is the ratio of peak forcing acceleration relative to gravity. In both the inviscid (Benjamin & Ursell 1954) and viscous (Kumar & Tuckerman 1994; Kumar 1996) cases, a spectral decomposition yields a system of Mathieu equations, whose stability depends on $\Gamma > 0$. In the dissipative case, the surface destabilises at $\Gamma = \Gamma_F$ (the Faraday threshold), which corresponds to the critical wavenumber $k = k_F$ and subharmonic waves (relative to the forcing frequency).

In all non-coalescing states, the droplet and bath remain separated by a thin air lubrication layer (Walker 1978), where the air slowly escapes (Couder *et al.* 2005a). The restoring forces of the wave field transmitted through the lubrication layer propel the droplet back into the air before coalescence, leading to periodic bouncing. The bouncing threshold Γ_B has been investigated through lubrication theory (Gilet *et al.* 2008) and a spring model for droplet impact (Hubert *et al.* 2015).

For $\Gamma > \Gamma_B$, a range of bouncing dynamics occur, which destabilise to walking at $\Gamma = \Gamma_W > \Gamma_B$. The vertical dynamics of walkers are frequently observed to be in subharmonic resonance with the wave field, although a range of periodic and chaotic

dynamics exist. Following Gilet & Bush (2009), we distinguish different vertical
dynamics by (m, n), where m is the number of forcing periods and n is the number
of impacts for the dynamics to repeat. The aforementioned subharmonic $(2, 1)$ mode
has two distinct energy levels: the lower-energy $(2, 1)^1$ mode and the higher-energy
$(2, 1)^2$ mode observed at higher Γ, where the impact durations are much shorter. The
bifurcation to different (m, n) regimes as a function of droplet diameter and Γ/Γ_F
was recorded by Protière *et al.* (2006) and Eddi *et al.* (2008). However, Moláček &
Bush (2013a) showed that the bouncing thresholds for different fluids collapse onto
a single curve if the drops are instead characterised by their dimensionless vibration
number,

$$\Omega = \omega_0 \sqrt{\rho R_0^3/\sigma}, \tag{1.1}$$

where R_0 is the droplet radius, with fluid density ρ and surface tension σ. This is
the frequency ratio of bath vibrations to characteristic droplet oscillations. Regime
diagrams in the (Γ, Ω)-plane are found in Wind-Willassen *et al.* (2013).

Due to the complexity of this system, no unified model exists to describe all of the
observed dynamics. The first simple model captured the qualitative bifurcation from
bouncing to walking through a period-averaged differential equation for the droplet
position, but this was valid only in the low-memory limit and the $(2, 1)$ mode (Couder
et al. 2005b; Protière *et al.* 2006).

Assuming a linear wave field, Fort *et al.* (2010) modelled the wave field as a
superposition of exponentially decaying (in time) standing waves centred at each
(instantaneous) impact, with the droplet dynamics restricted to the predominant $(2, 1)$
mode. The wave field generated at each impact was the far-field approximation to
the Bessel function $J_0(k_F r)$ with an experimentally observed exponential spatial decay
correction. Although this model numerically verified the quantised orbits in a rotating
bath, it was not analysed mathematically, not least due to the spatial singularity
centred at each droplet impact.

With no spatial damping correction, Moláček & Bush (2013b) coupled the
wave dynamics with a logarithmic spring model for the vertical motion of the
droplet (Moláček & Bush 2013a). This model successfully predicts many of the
experimentally observed bouncing and walking (m, n) modes (Wind-Willassen
et al. 2013), but relies on experimentally fitted parameters and is too complex
for mathematical analysis.

To simplify this, Oza, Rosales & Bush (2013) observed that the time scale of
the horizontal motion is much greater than that of the vertical motion in the $(2, 1)$
mode. Under this assumption, they approximated the sum of instantaneous impacts
by a continuous integral, leading to an integro-differential trajectory equation for the
droplet, which records the entire path history of the droplet (unlike the low-memory
limit model of Protière *et al.* (2006)). This past behaviour can be approximated in
the small-acceleration limit, yielding a hydrodynamic boost factor for the droplet
mass from its wave field interaction (Bush, Oza & Moláček 2014). By studying
the trajectory equation, analytic expressions are obtained for the bifurcation from
bouncing to walking and the walking speed (Oza *et al.* 2013), circular orbits in
a rotating frame (Oza *et al.* 2014a) and circular orbits in a harmonic potential
(Labousse *et al.* 2016). Advantageously, the linear stability of these dynamics can be
obtained analytically from the trajectory equation.

The above models all have one fundamental shortcoming: they simplify the
complex wave field generated by each droplet impact by decoupling the radial
and temporal behaviour. To remedy this, Eddi *et al.* (2011) modelled the wave

field depression around the droplet during impact as a finite cap, which evolves under the wave dynamics of Benjamin & Ursell (1954) with a phenomenological viscous damping factor. As this model includes a range of wavenumbers (rather than just k_F), the experimentally observed spatial damping is automatically captured. As an alternative to computing the dynamics of many wavenumbers, Moláček & Bush (2013b) (non-rigorously) suggested that the single impact is $J_0(k_F r)$, spatially corrected by a radial Gaussian with a linear temporal decay length, and exponentially decaying in time. On superposition, the exponential spatial decay correction for the wave field of a bouncer is recovered (Damiano *et al.* 2016).

The approximations in the aforementioned models prevent their usage in two important situations: complex vertical droplet dynamics (without the restriction to the (2, 1) mode) and the effect of submerged topography. By adopting the theory of quasi-potential flow (Dias, Dyachenko & Zakharov 2008), coupled with the logarithmic spring model for the vertical dynamics of the droplet (Moláček & Bush 2013a), Milewski *et al.* (2015) accurately predicted the bifurcations between different bouncing and walking modes, and the observed exponential spatial damping, and, in principle, the model may be adapted for any geometry.

The model presented herein considers the accurate wave field model of Milewski *et al.* (2015) together with the simplifications of instantaneous and point impacts. In a sense, this is the opposite limit to the trajectory equation of Oza *et al.* (2013). In § 2, we present the wave field equations of Milewski *et al.* (2015) and droplet dynamics of Moláček & Bush (2013b). In § 3, we perform a basis function expansion to collapse the model to a system of Mathieu differential equations. Assuming instantaneous impacts, the wave and droplet dynamics are only computed at discrete times, and the full problem collapses to a discrete map, yielding efficient computation of the dynamics and definitive stability results for various states. We capture bouncing (§ 4) and walking states, and the bifurcation between them (§ 5). We explore the quantisations of orbiting and promenading pairs, with the first investigation of walking droplet trains (§ 6). Finally, we model circular orbits of a droplet in a harmonic potential and capture the double quantisation of Perrard *et al.* (2014b) via statistical methods in the chaotic regime (§ 7).

2. Model derivation

2.1. *Wave dynamics*

We employ the governing equations derived by Milewski *et al.* (2015), who considered an incompressible viscous fluid in an infinite domain, with a small vortical boundary layer at the surface. Since a bouncing droplet emits radially symmetric waves, it is natural to write the spatial system in cylindrical polar coordinates (r, θ, z). Assuming that the waves and fluid velocity are small with a shallow wave slope, the velocity potential $\phi(r, \theta, z, t)$ and wave perturbation $\eta(r, \theta, t)$ at time $t > 0$ satisfy the linearised system

$$0 = \nabla_H^2 \phi + \phi_{zz}, \quad z \leqslant 0, \tag{2.1}$$

$$\phi_t = -g_\Gamma(t)\eta + \frac{\sigma}{\rho}\nabla_H^2\eta + 2\nu\nabla_H^2\phi - \frac{1}{\rho}P(r, \theta, t), \quad z = 0, \tag{2.2}$$

$$\eta_t = \phi_z + 2\nu\nabla_H^2\eta, \quad z = 0, \tag{2.3}$$

with $\nabla\phi \to \mathbf{0}$ and $\eta \to 0$ in the far field. In the above, we have constant surface tension σ, density ρ and kinematic viscosity ν, where ∇_H^2 is the horizontal Laplacian.

In the vibrating frame, the effective gravity is $g_\Gamma(t) \equiv g(1 - \Gamma \cos(\omega_0 t))$, where $\omega_0/(2\pi)$ is the vibration frequency and Γ is the ratio of maximum vibration acceleration relative to gravity g. As the droplet impacts the surface, the externally applied pressure on the bath is given by $P(r, \theta, t)$, which we prescribe in § 3. Coupled with droplet dynamics, Milewski *et al.* (2015) solved this system numerically, but we make several simplifying assumptions to analyse a wide range of dynamics observed in an unbounded domain.

2.2. *Droplet dynamics*

By adapting the work of Moláček & Bush (2013*b*), we model the droplet dynamics as a rigid sphere of mass m under ballistic motion centred at the point $(\mathbf{x}, z) = (X(t), Z(t))$ in Cartesian coordinates. This neglects droplet deformation, which is a reasonable assumption for the small droplets considered (Moláček & Bush 2013*b*). During flight, the droplet experiences an aerodynamical force described by Stokes drag, namely $-\nu_p X'(t)$ and $-\nu_p Z'(t)$ in the horizontal and vertical directions respectively. Here, $\nu_p = 6\pi R_0 \mu_{air}$ for droplet radius R_0 and air viscosity μ_{air} (Moláček & Bush 2013*b*).

The droplet experiences a force of magnitude $f(t) \geqslant 0$ due to the lubrication air layer during impact ($f = 0$ during flight). As the droplet radius R_0 is much smaller than a typical wavelength λ ($R_0/\lambda \ll 1$), the forces experienced from the wave field interaction are localised to the point $\mathbf{x} = X(t)$ on the fluid surface. These are modelled as an impulsive force $f(t)\hat{\mathbf{n}}(X(t), t)$ and shear forces described by the *skidding friction* $-c\sqrt{\rho R_0/\sigma}f(t)X'(t)$. Here, $\hat{\mathbf{n}} = (-\nabla\eta, 1)/(1 + |\nabla\eta|^2)^{-1/2}$ is the unit normal away from the fluid surface and c is the dimensionless skidding friction coefficient introduced by Moláček & Bush (2013*b*) (this is discussed in § 3.3). As the fluid model assumes a shallow wave slope $|\nabla\eta| \ll 1$, we approximate $\hat{\mathbf{n}} \sim (-\nabla\eta, 1)$.

For analogies to quantum mechanics, experiments are construed to subject the horizontal motion of the droplet to an external potential $\mathcal{V}(X(t), t)$, such as the dynamics in a rotating bath (Fort *et al.* 2010) and a horizontal harmonic potential well (Perrard *et al.* 2014*b*). On combining these forces, conservation of momentum supplies

$$mX''(t) + c\sqrt{\rho R_0/\sigma}f(t)X'(t) + \nu_p X'(t) = -\nabla\mathcal{V}(X(t), t) - f(t)\nabla\eta(X(t), t), \quad (2.4)$$

$$mZ''(t) + \nu_p Z'(t) = -mg_\Gamma(t) + f(t), \quad (2.5)$$

written in the vibrating frame. In what follows, we take $\mathcal{V} \equiv 0$ for free walking dynamics, or $\mathcal{V} = (1/2)\kappa|X(t)|^2$ for dynamics in a harmonic potential well with an adjustable spring constant $\kappa \geqslant 0$. The analysis for other potentials follows akin to this work.

For simplicity, we assume that the bouncing droplet lies in the prevalent $(2, 1)$ mode, which implies that both $Z(t)$ and $f(t)$ are periodic with subharmonic period $T = 4\pi/\omega_0$. By integrating (2.5) over an impact period and exploiting periodicity, $f(t)$ must satisfy

$$mgT = \int_\tau^{\tau+T} f(t)\, dt, \quad \forall\tau \geqslant 0, \quad (2.6)$$

as derived by Moláček & Bush (2013*b*). Although we could carefully model the force $f(t)$ as a response to the impact dynamics (e.g. as a logarithmic spring (Moláček & Bush 2013*a*)), we use condition (2.6) to prescribe a reasonable choice of $f(t)$ in § 3.2.

Variable	Value	Description
σ	2.06×10^{-2} kg s^{-2}	Surface tension
ρ	949 kg m^{-3}	Fluid density
ν	2×10^{-5} m^2 s^{-1}	Kinematic viscosity (fluid)
μ_{air}	1.8×10^{-5} kg m^{-1} s^{-1}	Dynamic viscosity (air)
g	9.8 m s^{-2}	Gravity
ω_0	$80 \times 2\pi$ s^{-1}	Vibration frequency ($\times 2\pi$)
R_0	3.8×10^{-4} m	Droplet radius
m	2.2×10^{-7} kg	Droplet mass
ν_p	1.3×10^{-7} kg s^{-1}	Stokes drag on droplet

TABLE 1. Fixed variables used in this model.

3. Model reduction

For mathematical analysis, we non-dimensionalise the governing equations (2.1)–(2.4) and condition (2.6). We rescale the lengths to a typical wavelength $\lambda = 0.51$ cm and time to the subharmonic bouncing period $T = 4\pi/\omega_0$, with balances $f \sim mg$ and $P \sim mg/\lambda^2$. This yields the dimensionless equations for the waves,

$$0 = \nabla_H^2 \phi + \phi_{zz}, \quad z \leqslant 0, \tag{3.1}$$

$$\phi_t = -G\tilde{g}_\Gamma(t)\eta + B\nabla_H^2\eta + 2\epsilon\nabla_H^2\phi - MGP(r, \theta, t), \quad z = 0, \tag{3.2}$$

$$\eta_t = \phi_z + 2\epsilon\nabla_H^2\eta, \quad z = 0, \tag{3.3}$$

and droplet dynamics,

$$X''(t) = -c\sqrt{\frac{R}{B}}Gf(t)X'(t) - \tilde{\nu}_p X'(t) - \tilde{\kappa}X(t) - Gf(t)\nabla\eta(X(t), t), \tag{3.4}$$

$$1 = \int_\tau^{\tau+1} f(t)\,\mathrm{d}t, \tag{3.5}$$

for any $\tau > 0$. Here, we have defined dimensionless parameters

$$\epsilon = \frac{\nu T}{\lambda^2}, \quad B = \frac{\sigma T^2}{\rho\lambda^3}, \quad G = \frac{gT^2}{\lambda}, \quad M = \frac{m}{\rho\lambda^3}, \quad R = \frac{R_0}{\lambda}, \quad \tilde{\nu}_p = \frac{\nu_p T}{m}, \quad \tilde{\kappa} = \frac{\kappa T^2}{m}. \tag{3.6a-g}$$

Typical parameter values from table 1 give a reciprocal Reynolds number of $\epsilon \approx 0.019$, a Bond number of $B \approx 0.102$, $G \approx 1.201$, $M \approx 0.0017$, $R \approx 0.075$ and $\tilde{\nu}_p \approx 0.01$. The droplet radius corresponds to a vibration number of $\Omega \equiv 4\pi\sqrt{R^3/B} = 0.8$, which minimises the walking threshold Γ_W for this fluid (Wind-Willassen *et al.* 2013). The dimensionless potential strength $\tilde{\kappa} \sim 10^{-2}$ is a free parameter of both the model and experiments.

As we prescribe the periodic vertical dynamics, we must prescribe the phase shift β between the vertical motion of the droplet and the waves (this is discussed in § 3.3). This alters the dimensionless effective gravity to $\tilde{g}_\Gamma(t) = 1 - \Gamma\cos(4\pi t + \beta)$.

3.1. *Basis function expansion*

The assumption of infinite depth allows us to adapt the ideas of Benjamin & Ursell (1954), whereby we decompose the wave perturbation η and velocity potential ϕ in terms of orthogonal eigenfunctions of Laplace's equation. Specifically, we use Bessel functions $J_m(\cdot)$ to pose the expansions

$$\eta(r,\theta,t) = \sum_{m=0}^{\infty} \int_0^{\infty} k(a_m(t;k)\Phi_m(r,\theta;k) + b_m(t;k)\Psi_m(r,\theta;k))\,\mathrm{d}k, \qquad (3.7)$$

$$\phi(r,\theta,z,t) = \sum_{m=0}^{\infty} \int_0^{\infty} k\mathrm{e}^{kz}(c_m(t;k)\Phi_m(r,\theta;k) + d_m(t;k)\Psi_m(r,\theta;k))\,\mathrm{d}k, \qquad (3.8)$$

where $\Phi_m(r,\theta;k) \equiv J_m(kr)\cos(m\theta)$ and $\Psi_m(r,\theta;k) \equiv J_m(kr)\sin(m\theta)$ satisfy

$$\nabla_H^2 \Phi_m(r,\theta;k) = -k^2\Phi_m(r,\theta;k) \quad \text{and} \quad \nabla_H^2\Psi_m(r,\theta;k) = -k^2\Psi_m(r,\theta;k). \qquad (3.9a,b)$$

The coefficients a_m, b_m, c_m and d_m may be determined on substitution into (3.1)–(3.3). For clarity, we set $b_0 \equiv d_0 \equiv 0$ since $\Psi_0(r,\theta;k) \equiv 0$ for all $k \geqslant 0$.

By choice of the orthogonal basis functions in (3.8), the continuity equation (2.1) is automatically satisfied. For horizontal droplet position $(r,\theta) = (r_d(t),\theta_d(t))$ at time $t > 0$ and small droplets, we model the droplet impacts at a point. Thus, we prescribe the pressure

$$P(r,\theta,t) = f(t)\frac{1}{r}\delta(r - r_d(t))\delta(\theta - \theta_d(t)), \qquad (3.10)$$

where $f(t)$ is the force applied by the droplet on the surface, which is zero during droplet flight. By exploiting the closure relation $\int_0^{\infty} kr J_m(kr)J_m(\xi r)\,\mathrm{d}r = \delta(k - \xi)$ and trigonometric orthogonality, we expand

$$P(r,\theta,t) = \sum_{m=0}^{\infty} \int_0^{\infty} k(p_m(t;k)\Phi_m(r,\theta;k) + q_m(t;k)\Psi_m(r,\theta;k))\,\mathrm{d}k, \qquad (3.11)$$

where

$$p_m(t;k) = \frac{1}{W_m}f(t)\Phi_m(r_d(t),\theta_d(t);k) \quad \text{and} \quad q_m(t;k) = \frac{1}{W_m}f(t)\Psi_m(r_d(t),\theta_d(t);k), \qquad (3.12a,b)$$

with eigenfunction norms $W_m = \pi$ if $m > 0$ and $W_0 = 2\pi$. It should be noted that $q_0 \equiv 0$.

We substitute (3.7)–(3.11) into (3.2)–(3.3) and eliminate c_m and d_m in favour of a_m and b_m. By orthogonality, we obtain a system of inhomogeneous damped Mathieu equations,

$$\mathcal{L}_k a_m(t;k) = -kMG p_m(t;k) \quad \text{and} \quad \mathcal{L}_k b_m(t;k) = -kMG q_m(t;k), \qquad (3.13a,b)$$

where

$$\mathcal{L}_k \equiv \partial_{tt} + 2\gamma(k)\partial_t + (\gamma^2(k) + \omega^2(k) - \Gamma\omega_g^2(k)\cos(4\pi t + \beta)) \qquad (3.14)$$

is the wavenumber-dependent homogeneous damped Mathieu differential operator and

$$\gamma(k) \equiv 2\epsilon k^2, \quad \omega^2(k) \equiv Gk + Bk^3, \quad \omega_g^2(k) \equiv Gk. \qquad (3.15a\text{–}c)$$

The $\gamma^2(k)$ term gives the additional damping from the vortical boundary layer; this is not present in the work of Eddi *et al.* (2011), who instead replace ϵ with a phenomenological damping term to match the Faraday threshold.

3.2. *Instantaneous impacts*

To close the system, it remains to prescribe $f(t)$ so that (3.5) is satisfied. To alleviate the difficulty of analysing inhomogeneous Mathieu equations, we simply model the impacts as instantaneous. This gives homogeneous equations for the waves and droplet during flight, and jump conditions at impact. This is the opposite limit to that of Oza *et al.* (2013), where the droplet glides across the surface of the bath with constant forcing $f(t)$. Assuming that the first impact is at $t = 0$, we define

$$f(t) = \sum_{n=0}^{\infty} \delta(t - t_n), \tag{3.16}$$

where $t_n \equiv n$ for all non-negative integers n and $\delta(\cdot)$ is the Dirac delta function. This satisfies periodicity and the integral condition (3.5). We now exploit properties of $\delta(\cdot)$ to replace the inhomogeneities in (3.13) with jump conditions.

For physical consistency, we assume that the droplet position $X(t)$ and wave amplitudes ($a_m(t; k)$ and $b_m(t; k)$) are continuous across all impacts. We denote jumps $[Q(t_n)]_-^+ \equiv Q(t_n^+) - Q(t_n^-)$ for any function of time $Q(t)$, where t_n^+ and t_n^- are the right and left limits of t_n respectively. We now integrate the governing equations (3.13) over $t \in [t_n^-, t_n^+]$. For all $n \geqslant 0$, the first equation gives

$$\int_{t_n^-}^{t_n^+} \mathcal{L}_k a_m(t; k) \, \mathrm{d}t = \frac{-k}{W_m} MG \int_{t_n^-}^{t_n^+} \delta(t - t_n) \Phi_m(r_d(t), \theta_d(t); k) \, \mathrm{d}t. \tag{3.17}$$

As the droplet position is assumed to be continuous, the sifting property of $\delta(\cdot)$ can be applied to the right-hand side. We use the continuity of $a_m(t; k)$ to simplify the left-hand side. Hence, (3.13) supply jump conditions

$$[a_m'(t_n; k)]_-^+ = -P_m(k) \Phi_m(r_d(t_n), \theta_d(t_n); k), \tag{3.18}$$

$$[b_m'(t_n; k)]_-^+ = -P_m(k) \Psi_m(r_d(t_n), \theta_d(t_n); k), \tag{3.19}$$

where a prime denotes the partial derivative with respect to t and $P_m(k) = kMG/W_m$.

For the droplet dynamics (3.4), we first consider a single impact at $t = t_\star$. Hence,

$$X''(t) + c\sqrt{R/B} G\delta(t - t_\star)X'(t) + \tilde{\nu}_p X'(t) + \tilde{\kappa}X(t) = -G\delta(t - t_\star)\nabla\eta(X(t), t). \tag{3.20}$$

For $c = 0$, we may proceed as above to find the jump in $X'(t)$ at $t = t_\star$. The case $c > 0$ is more delicate; the sifting property cannot be applied as $X'(t)$ is discontinuous at $t = t_\star$. Following the method of Catllá *et al.* (2008), we replace $\delta(t - t_\star)$ with

$$\delta_\varepsilon(t - t_\star) \equiv \varepsilon^{-1} \varphi((t - t_\star)\varepsilon^{-1}), \quad \forall \varepsilon > 0, \tag{3.21}$$

where $\varphi(\tau) \geqslant 0$ for all $\tau \in \mathbb{R}$ and $\int_{-\infty}^{\infty} \varphi(\tau) \, \mathrm{d}\tau = 1$. Hence, the functions $\delta_\varepsilon(\cdot) \to \delta(\cdot)$ pointwise as $\varepsilon \to 0$, except at the jump discontinuity in $\delta(\cdot)$. This is an appealing formulation, as, physically, no impact is actually instantaneous – it just occurs over a much faster time scale than the dynamics of the rest of the system.

The idea is to find a solution to (3.20) when $t > t_\star$ with $\delta(\cdot)$ replaced by $\delta_\varepsilon(\cdot)$, and then consider the limit as $\varepsilon \to 0$. This determines $X'(t_\star^+)$. However, for $t < t_\star$, (3.20) can be solved directly without approximation (as the $\delta(\cdot)$ terms vanish), which supplies $X'(t_\star^-)$. Hence, the jump $[X'(t_\star)]_-^+$ is obtained, which is independent of $\varphi(\cdot)$. By generalising the proof of Catllá *et al.* (2008) (as outlined in appendix A) and extending to periodic impacts, we obtain the jump condition shown in (3.27) below.

3.3. *Model summary*

We have the dimensionless system

$$0 = \mathcal{L}_k a_m(t; k), \quad \forall t \neq t_n, \tag{3.22}$$

$$0 = \mathcal{L}_k b_m(t; k), \quad \forall t \neq t_n, \tag{3.23}$$

$$\mathbf{0} = \mathbf{X}''(t) + \tilde{\nu}_p \mathbf{X}'(t) + \tilde{\kappa} \mathbf{X}(t), \quad \forall t \neq t_n, \tag{3.24}$$

$$[a_m'(t_n; k)]_-^+ = -P_m(k)\Phi_m(\mathbf{X}(t_n); k), \tag{3.25}$$

$$[b_m'(t_n; k)]_-^+ = -P_m(k)\Psi_m(\mathbf{X}(t_n); k), \tag{3.26}$$

$$[\mathbf{X}'(t_n)]_-^+ = -F(c)\left(\frac{1}{c}\sqrt{\frac{B}{R}}\nabla\eta(\mathbf{X}(t_n), t_n) + \mathbf{X}'(t_n^-)\right), \tag{3.27}$$

where $P_m(k) = kMG/W_m$ and $F(c) = 1 - \exp(-cG\sqrt{R/B})$. One should note the abuse of notation $\Phi_m(\mathbf{X}(t_n); k) \equiv \Phi_m(r_d(t_n), \theta_d(t_n); k)$ (and similarly for Ψ_m). The system of jump conditions is self-consistent, with both η and $\mathbf{X}$ continuous across impacts.

This model has two undefined parameters: the skidding friction c and the phase shift β. From the theoretical calculations of Moláček & Bush (2013*b*), $c \approx 0.3$, but the authors consider $c \in [0.17, 0.33]$ for simulations. Oza *et al.* (2013) use the lower bound $c = 0.17$ in the stroboscopic approximation model, which has the opposite impact duration limit to our model. Hence, it is natural to choose the upper bound $c = 0.33$, which is fixed throughout the paper. The phase shift β between bath vibrations and droplet impacts for periodic states arises naturally in models where the droplet vertical dynamics are explicitly modelled (Moláček & Bush 2013*b*; Milewski *et al.* 2015). As we restrict the droplet to periodic impacts, we must choose β. We focus on the prevalent $(2, 1)^2$ walking mode, where β has a typical value of $\beta = \pi$ (Milewski *et al.* 2015), which is fixed henceforth. For later works, c and β may be tuned when comparing with experimental data.

3.4. *Faraday instability*

Following Milewski *et al.* (2015) to determine the subharmonic Faraday instability, we look for subharmonic solutions to $\mathcal{L}_k a(t; k) = 0$ of the form $a(t; k) = A\cos(2\pi t) + B\sin(2\pi t)$. After substitution, higher-order frequencies are neglected, which is equivalent to truncating the Hill matrix. For a non-trivial system, we require

$$(w^2(k) + \gamma^2(k) - 4\pi^2)^2 + 16\pi^2\gamma^2(k) - \tfrac{1}{4}w_g^4(k)\Gamma^2 = 0. \tag{3.28}$$

The function $\Gamma = \Gamma(k)$ is globally minimised at $k = k_F$, where for $\Gamma < \Gamma(k_F) \equiv \Gamma_F$ the subharmonic solutions are stable for any $k > 0$. By our dimensionless scaling, $\lambda_F \approx 1$, where $k_F = 2\pi/\lambda_F$. Although it is known that Γ_F obtained in this model is not accurate when compared with experiments (Milewski *et al.* 2015), it is usual to use Γ/Γ_F as a controlling parameter (Eddi *et al.* 2011). In fact, we show in §5.3 that the wave field temporal decay rate may be written as a function of Γ/Γ_F, which justifies our approach for a theoretical investigation.

3.5. *Discrete-time model*

As (3.22)–(3.27) form a homogeneous system with jump conditions, it is natural to reformulate as a discrete-time system. We denote $\boldsymbol{a}_n(k) \equiv (a_0(t_n; k), a_1(t_n; k), \ldots)^{\mathrm{T}}$ and $\boldsymbol{a}_n'(k) \equiv (a_0'(t_n^+; k), a_1'(t_n^+; k), \ldots)^{\mathrm{T}}$, and similarly for $\boldsymbol{b}_n(k)$ and $\boldsymbol{b}_n'(k)$. We also write the

eigenfunctions as vectors $\boldsymbol{\Phi}(\cdot;k) = (\Phi_0(\cdot;k), \Phi_1(\cdot;k), \ldots)^{\mathrm{T}}$, and similarly for $\boldsymbol{\Psi}(\cdot;k)$, with $\boldsymbol{P}(k)$ a diagonal matrix with elements $P_m(k)$. By periodicity of the Mathieu operator $\mathcal{L}_k$, we numerically construct the principal fundamental matrix $\boldsymbol{M}_k(\Gamma)$ over the interval $(0, 1)$. As $\mathcal{L}_k$ is independent of the Bessel order, $\boldsymbol{M}_k$ has block diagonal form

$$\boldsymbol{M}_k(\Gamma) = \begin{bmatrix} m_{11}(\Gamma;k)\boldsymbol{I} & m_{12}(\Gamma;k)\boldsymbol{I} \\ m_{21}(\Gamma;k)\boldsymbol{I} & m_{22}(\Gamma;k)\boldsymbol{I} \end{bmatrix}, \tag{3.29}$$

where $\boldsymbol{I}$ is the infinite identity matrix. The principal fundamental matrix $\boldsymbol{F}(\tilde{\kappa})$ corresponding to the droplet dynamics is constructed by analytically solving (3.24).

We reformulate (3.22)–(3.27) as an efficient one-step map with stages for droplet position $\boldsymbol{X}_n \equiv \boldsymbol{X}(t_n)$ and velocity $\boldsymbol{X}'_n \equiv \boldsymbol{X}'(t_n^+)$.

(i) Use $\boldsymbol{X}_n$ and $\boldsymbol{X}'_n$ to compute $\boldsymbol{X}_{n+1}$ and $\tilde{\boldsymbol{X}}' \equiv \boldsymbol{X}'(t_{n+1}^-)$:

$$\begin{bmatrix} \boldsymbol{X}_{n+1} \\ \tilde{\boldsymbol{X}}' \end{bmatrix} = \boldsymbol{F}(\tilde{\kappa}) \begin{bmatrix} \boldsymbol{X}_n \\ \boldsymbol{X}'_n \end{bmatrix}. \tag{3.30}$$

(ii) Update wave amplitudes including jump conditions $\forall k > 0$ (similarly for $\boldsymbol{b}_n(k)$):

$$\begin{bmatrix} \boldsymbol{a}_{n+1}(k) \\ \boldsymbol{a}'_{n+1}(k) \end{bmatrix} = \boldsymbol{M}_k(\Gamma) \begin{bmatrix} \boldsymbol{a}_n(k) \\ \boldsymbol{a}'_n(k) \end{bmatrix} - \begin{bmatrix} \boldsymbol{0} \\ \boldsymbol{P}(k)\boldsymbol{\Phi}(\boldsymbol{X}_{n+1};k) \end{bmatrix}. \tag{3.31}$$

(iii) Apply droplet jump conditions:

$$\boldsymbol{X}'_{n+1} = (1 - F(c))\tilde{\boldsymbol{X}}' - \frac{F(c)}{c}\sqrt{\frac{B}{R}}\boldsymbol{\nabla}\eta(\boldsymbol{X}_{n+1}, t_{n+1}). \tag{3.32}$$

3.6. *Numerical implementation*

The remainder of this work involves simulating and finding fixed points of the system (3.30)–(3.32), both of which require suitable truncations in the wavenumber $k > 0$ and Bessel mode $m \in \mathbb{N}$. For any impact time t_n, the wavenumbers are generally peaked around $k = k_F$, with the peak becoming narrower as $\Gamma \to \Gamma_F^-$, which can be analysed from Floquet analysis of the damped Mathieu equation. This determines the refinement and truncation in k, which is successively reduced until the change in the numerical solution of the fixed points becomes negligible. Away from the Faraday threshold, a reasonably coarse mesh is sufficient, with $\delta k \sim 0.2$ and $k \in [k_F/2, 3k_F/2]$, where k_F is a mesh point. Integrals over k (e.g. for finding $\nabla\eta$) are evaluated using the trapezium rule, which is well suited to capturing the peaked behaviour in k.

Truncation of the Bessel modes follows from the asymptotic behaviour of Bessel functions, namely $\mathrm{J}_m(z) \sim (1/m!)(z/2)^m$ for $0 < z \ll \sqrt{m+1}$. Hence, for orbital solutions or simulations with a central force, the maximum radial extent of the droplet can be estimated, which provides a good guide for the truncation $m \in \{0, 1, \ldots, m^\star\}$. For walking dynamics, the Floquet exponents provide an estimate of how the temporal decay affects the number of past impacts that contribute to the current wave field (this is the system 'memory', as discussed in § 5.3), where we typically have $m^\star = 15$ for $\Gamma/\Gamma_F \approx 0.81$ but $m^\star \approx 50$ for $\Gamma/\Gamma_F \approx 0.95$. The accuracy of this truncation can be easily checked *a posteriori*, with $m^\star$ increased until there is a negligible change in the numerical solution.

For simulation efficiency, Bessel functions are only evaluated once per impact period, with derivatives calculated using the identity $\mathrm{J}'_m(z) = (1/2)(\mathrm{J}_{m-1}(z) - \mathrm{J}_{m+1}(z))$. We typically simulate 1000 impacts per second on a standard desktop machine using MATLAB.

4. Bouncing states

We now find bouncing states of (3.22)–(3.27) with $\tilde{\kappa} = 0$. By translational invariance, we assume that the drop bounces at the origin ($X \equiv 0$) with radially symmetric wave field

$$\eta(r, t) = \int_0^\infty k a_0(t; k) \mathrm{J}_0(kr) \, \mathrm{d}k. \tag{4.1}$$

This ensures that the droplet receives no horizontal kick at impact, and so remains a bouncer. We demand a periodic wave field, with $\eta(\mathbf{x}, t_{n+1}) = \eta(\mathbf{x}, t_n)$ and $\eta_t(\mathbf{x}, t_{n+1}^+) = \eta_t(\mathbf{x}, t_n^+)$ for all n and all $\mathbf{x} \in \mathbb{R}^2$. By orthogonality, the wave amplitudes must satisfy

$$a_0(t_{n+1}; k) = a_0(t_n; k), \tag{4.2}$$
$$a_0'(t_{n+1}^+; k) = a_0'(t_n^+; k), \tag{4.3}$$

for all t_n and $\forall k \geqslant 0$. By periodicity, it is sufficient to consider the interval $t \in [0, 1]$.

By considering (3.31) and the form of $\mathbf{M}_k(\Gamma)$, it remains to solve the linear system

$$\left(\mathbf{I}_2 - \begin{bmatrix} m_{11}(\Gamma; k) & m_{12}(\Gamma; k) \\ m_{21}(\Gamma; k) & m_{22}(\Gamma; k) \end{bmatrix} \right) \begin{bmatrix} a_0(0; k) \\ a_0'(0^+; k) \end{bmatrix} = \begin{bmatrix} 0 \\ -P_0(k) \end{bmatrix}, \tag{4.4}$$

where $\mathbf{I}_2 \in \mathbb{R}^{2 \times 2}$ is the identity matrix and we used $\Phi_0(\mathbf{0}; k) = 1$, $\forall k$.

4.1. *Stability analysis*

To determine the walking threshold $\Gamma = \Gamma_W$, we perform linear stability analysis of the periodic bouncing system. The aim is to construct a one-step matrix map $\mathbf{T}(\Gamma)$ for the perturbed system, where stability is determined by the spectral radius $\rho(\mathbf{T})$. We denote the steady state by $X = \hat{X}$, $a_m = \hat{a}_m$ and $b_m = \hat{b}_m$, where, for bouncing at the origin, $\hat{X} \equiv \mathbf{0}$, $\hat{a}_m \equiv \hat{b}_m \equiv 0$ for all $m \geqslant 1$, and $\hat{b}_0 \equiv 0$. We then consider small perturbations

$$X(t) = \hat{X}(t) + \boldsymbol{\epsilon}(t), \quad a_m(t; k) = \hat{a}_m(t; k) + \tilde{a}_m(t; k), \quad b_m(t; k) = \hat{b}_m(t; k) + \tilde{b}_m(t; k), \tag{4.5a-c}$$

where we assume that $|\tilde{a}_m/\hat{a}_0| \sim |\tilde{b}_m/\hat{a}_0| \sim \|\boldsymbol{\epsilon}\| \ll 1$. By including an explicit perturbation to the wave field, we consider a more general perturbation than Oza *et al.* (2013).

The system is linearised via the jump conditions (3.25)–(3.27), giving

$$[\tilde{a}_m'(t_n; k)]_-^+ = -P_m(k) \nabla \Phi_m(\mathbf{0}; k)^\mathrm{T} \boldsymbol{\epsilon}(t_n), \tag{4.6}$$
$$[\tilde{b}_m'(t_n; k)]_-^+ = -P_m(k) \nabla \Psi_m(\mathbf{0}; k)^\mathrm{T} \boldsymbol{\epsilon}(t_n), \tag{4.7}$$
$$[\boldsymbol{\epsilon}'(t_n)]_-^+ = -F(c) \left(\boldsymbol{\epsilon}'(t_n^-) + \frac{1}{c} \sqrt{\frac{B}{R}} (\mathbf{H}(\Gamma) \boldsymbol{\epsilon}(t_n) + \nabla \tilde{\eta}(\mathbf{0}, t_n)) \right). \tag{4.8}$$

The Hessian matrix of the steady-state wave field at droplet impact is $\mathbf{H}(\Gamma)$ and

$$\nabla \tilde{\eta}(\mathbf{0}, t_n) = \sum_{m=0}^\infty \int_0^\infty k(\tilde{a}_m(t_n; k) \nabla \Phi_m(\mathbf{0}; k) + \tilde{b}_m(t_n; k) \nabla \Psi_m(\mathbf{0}; k)) \, \mathrm{d}k. \tag{4.9}$$

Equations (4.6)–(4.8) are simplified considerably by noting that

$$\nabla\Phi_1(\mathbf{0}; k) = (k/2, 0)^{\mathrm{T}}, \quad \nabla\Psi_1(\mathbf{0}; k) = (0, k/2)^{\mathrm{T}}, \quad \nabla\Phi_m(\mathbf{0}; k) \equiv \nabla\Psi_m(\mathbf{0}; k) \equiv \mathbf{0},$$
$$(4.10a{-}c)$$

for $m \neq 1$. Hence, for $m \neq 1$, the jump conditions for $\tilde{a}_m$, $\tilde{b}_m$ and $\boldsymbol{\epsilon}$ are all independent of each other (to $O(\|\boldsymbol{\epsilon}\|)$). Therefore, the perturbations $\tilde{a}_m$, $\tilde{b}_m$ ($m \neq 1$) each decouple from the system. As they are unexcited solutions to the damped Mathieu equation with $\Gamma < \Gamma_F$, they are stable and hence are neglected from the stability analysis.

Using the linearised jump conditions with matrices $\mathbf{M}_k(\Gamma)$ and $\mathbf{F}(0)$, we construct a discrete-time linear map for all variables, given by the matrix $\mathbf{T}(\Gamma)$. The system is neutrally stable if the spectral radius $\rho(\mathbf{T}) = 1$, and unstable if $\rho(\mathbf{T}) > 1$. The walking threshold Γ_W is the largest Γ such that $\rho(\mathbf{T}) = 1$. By the translational invariance of the system, there always exists an eigenvalue μ of $\mathbf{T}$ such that $\mu = 1$, which prevents us from obtaining asymptotically stable solutions ($\rho(\mathbf{T}) < 1$) in the absence of a central force.

5. Steady walking states

By extension, we now find steady walking states and analyse their stability. By rotational and translational invariance, we consider steady walking along the x-axis in the direction of increasing x, with $X(t_0) = \mathbf{0}$ ($t_0 = 0$). By symmetry, $b_m \equiv 0$, $\forall m$.

We denote $0 < \delta x \equiv X(t_{n+1}) - X(t_n)$ for all t_n, where $X(t) = (X(t), 0)$. For the wave field to follow the droplet between impacts, Graf's addition theorem (Abramowitz & Stegun 1964) supplies the requirement

$$a_0(t_{n+1}; k) = \sum_{p=0}^{\infty} (-1)^p \mathrm{J}_p(k\delta x) a_p(t_n; k), \tag{5.1}$$

$$\forall m \geqslant 1: \quad a_m(t_{n+1}; k) = \sum_{p=0}^{\infty} (\mathrm{J}_{m-p}(k\delta x) + (-1)^p \mathrm{J}_{m+p}(k\delta x)) a_p(t_n; k), \tag{5.2}$$

and similarly for the first time derivatives. Hence, we have a discrete-time map

$$\mathbf{a}_{n+1}(k) = \mathbf{A}(k; \delta x)\mathbf{a}_n(k), \tag{5.3}$$

$$\mathbf{a}'_{n+1}(k) = \mathbf{A}(k; \delta x)\mathbf{a}'_n(k), \tag{5.4}$$

where $\mathbf{A}(k; \delta x)$ is an infinite matrix given by (5.1)–(5.2). As $\mathbf{A}(k; 0) = \mathbf{I}$, (5.3)–(5.4) simplify to the periodicity requirement (4.2)–(4.3) for a bouncing droplet.

For steady walking, we require $\mathbf{X}'(t_n^+) = \mathbf{V}_0 \equiv (V, 0)$ for all t_n, for some unknown $V > 0$. Solving (3.24) with $\tilde{\kappa} = 0$ for $t \in [t_n, t_{n+1})$ gives

$$\mathbf{X}(t_{n+1}) = \mathbf{X}(t_n) + \tilde{\nu}_p^{-1}(1 - \mathrm{e}^{-\tilde{\nu}_p})\mathbf{V}_0, \tag{5.5}$$

$$\mathbf{X}'(t_{n+1}^-) = \mathrm{e}^{-\tilde{\nu}_p}\mathbf{V}_0. \tag{5.6}$$

For $\mathbf{X}'(t_{n+1}^+) = \mathbf{V}_0$, the jump condition (3.27) and (5.6) give the requirement

$$\mathbf{V}_0 = (1 - F(c))\mathrm{e}^{-\tilde{\nu}_p}\mathbf{V}_0 - \frac{F(c)}{c}\sqrt{\frac{B}{R}}\nabla\eta(\mathbf{X}(t_{n+1}), t_{n+1}). \tag{5.7}$$

By the assumed periodicity of the wave field when centred at the droplet, $\nabla \eta(X(t_n), t_n)$ is constant for all t_n. Hence, using (4.10) to simplify the wave field gradient, we require

$$V_0 = \frac{-1}{1 - \mathrm{e}^{-\tilde{v}_p}(1 - F(c))} \frac{F(c)}{c} \sqrt{\frac{B}{R}} \int_0^\infty k a_1(0; k) \nabla \Phi_1(\mathbf{0}; k) \, \mathrm{d}k, \qquad (5.8)$$

where $\nabla \Phi_1(\mathbf{0}; k) = (k/2, 0)^{\mathrm{T}}$. From the x-components of (5.5) and (5.8), δx must satisfy

$$\delta x = \frac{-\tilde{v}_p^{-1}(1 - \mathrm{e}^{-\tilde{v}_p})}{1 - \mathrm{e}^{-\tilde{v}_p}(1 - F(c))} \frac{F(c)}{c} \sqrt{\frac{B}{R}} \int_0^\infty \frac{k^2}{2} a_1(0; k) \, \mathrm{d}k. \qquad (5.9)$$

To progress, we use the discrete map for the wave amplitudes (3.31). By periodicity and translational invariance, it is sufficient to consider $t \in [0, 1]$. Conditions (5.3)–(5.4) are thus equivalent to solving the linear system

$$\left(\begin{bmatrix} \mathbf{A}(k; \delta x) & \mathbf{0} \\ \mathbf{0} & \mathbf{A}(k; \delta x) \end{bmatrix} - \mathbf{M}_k(\Gamma) \right) \begin{bmatrix} \mathbf{a}_0(k) \\ \mathbf{a}_0'(k) \end{bmatrix} = - \begin{bmatrix} \mathbf{0} \\ \mathbf{P}(k) \Phi([\delta x, 0]^{\mathrm{T}}; k) \end{bmatrix}, \qquad (5.10)$$

for all $k \geqslant 0$, where δx is determined by (5.9). The block matrix form of this system allows for quick numerical solution, with the walking speed δx shown in figure 1(*a*).

To shed light on this bifurcation, we consider the average energy of the wave field across one period. As derived in appendix B, we compute the change in energy due to the existence of the waves formed by the droplet. This cannot be computed in the models of Moláček & Bush (2013*b*) and Oza *et al.* (2013), as the single-wavenumber (k_F) approximation gives insufficient decay at infinity. The dimensionless energy perturbation E as given in (B 7) is shown in figure 1(*b*), demonstrating that the wave field of a walker requires less energy than that of the corresponding unstable bouncer. We neglect the horizontal kinetic energy of the droplet as it is significantly smaller than the wave field energy for all walking speeds. Furthermore, the assumed periodicity of $Z(t)$ gives a constant droplet vertical energy (which balances the wave field energy) for both bouncing and walking.

5.1. *Stability analysis*

The stability analysis of a walker is similar to that of a bouncer and therefore we do not give the details. The main difference is that we use Graf's addition theorem (Abramowitz & Stegun 1964) to map the wave amplitude perturbation variables so that they are centred on the steady-state droplet position at each impact.

Following Oza *et al.* (2013), we consider general perturbations, and perturbations to the droplet in the direction of motion. In the former case, the walking is unstable. Physically, this corresponds to a new walker forming after an initial transient, but in a new direction. The latter case is achieved by noting that $\Psi_m \equiv 0$ along the x-axis, so the linearised jumps for the perturbation coefficients $\tilde{b}_m$ will be zero for an in-line perturbation. Furthermore, $\partial_x \Psi_m \equiv 0$ (for all m) along the x-axis, so the $\tilde{b}_m$ terms do not contribute to the linearised droplet perturbation jump condition. Hence, the $\tilde{b}_m$ terms decouple from the perturbed system and can be neglected as they are stable solutions to the Mathieu equation. In this case, the walker is neutrally stable, where an eigenvalue of 1 always exists due to the translational invariance of the problem. This agrees with experiments and also the model of Oza *et al.* (2013), whose analysis is restricted to lateral and in-line perturbations.
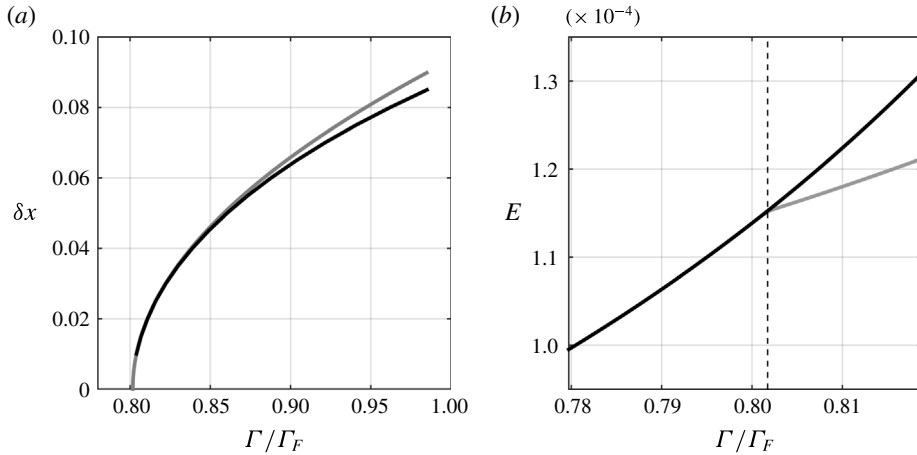
FIGURE 1. (*a*) Average walking speed δx for complete numerical method (black) and approximation valid only for $0 < \delta x \ll 1$ (grey). By the non-dimensionalisation, δx is the average walking speed relative to the phase speed of the waves. (*b*) The average wave field energy for a bouncer (black) and walker (grey), with a bifurcation at $\Gamma = \Gamma_W$.

5.2. *Slow-walking analysis*

As observed by Protière *et al.* (2006), there is a supercritical bifurcation at the walking threshold, where the walking speed grows like $(\Gamma - \Gamma_W)^{1/2}$. This behaviour has been captured in the trajectory equation of Oza *et al.* (2013). We explore the slow-walking speed in terms of the distance between impacts δx, which is the average walking speed in dimensionless variables. For $0 < \delta x \ll 1$, we consider asymptotic expansions of the form

$$\Gamma = \Gamma_W + \delta x \Gamma_1 + \delta x^2 \Gamma_2 + \cdots, \tag{5.11}$$

$$a_m(t; k) = a_m^{(0)}(t; k) + \delta x a_m^{(1)}(t; k) + \delta x^2 a_m^{(2)}(t; k) + \cdots, \tag{5.12}$$

for all $m \geqslant 0$. By the Frobenius series for Bessel functions, we have

$$J_0(k\delta x) \sim 1 - \left(\frac{k}{2}\right)^2 \delta x^2 + O(\delta x^4), \tag{5.13a}$$

$$J_1(k\delta x) \sim \left(\frac{k}{2}\right) \delta x - \frac{1}{2}\left(\frac{k}{2}\right)^3 \delta x^3 + O(\delta x^5), \tag{5.13b}$$

$$J_2(k\delta x) \sim \frac{1}{2}\left(\frac{k}{2}\right)^2 \delta x^2 + O(\delta x^4), \quad J_3(k\delta x) \sim \frac{1}{6}\left(\frac{k}{2}\right)^3 \delta x^3 + O(\delta x^5). \tag{5.14a,b}$$

These expansions are valid for $k/2 = O(1)$. As the least-damped wavenumber k_F satisfies $k_F/2 \approx \pi = O(1)$, and wavenumbers far away from k_F correspond to negligible wave amplitudes, this assumption is valid. We prove that $\Gamma_1 = 0$ and verify numerically that $\Gamma_2 > 0$, which gives the desired bifurcation.

Substituting the asymptotic expansions into the map (5.1)–(5.2), the Mathieu equation (3.22) and jump condition (3.25), and equating powers of δx, a system of

differential equations with initial and jump conditions is obtained, all of the general form

$$\mathcal{L}_k^{\Gamma_W} a(t; k) = \mathcal{H}, \quad a(1; k) = a(0; k) + \mathcal{B}, \quad a'(1^+; k) = a'(0^+; k) + \mathcal{B}', \left.\right\} \\ [a'(1; k)]_-^+ = \mathcal{J}. \tag{5.15}$$

Here, $\mathcal{H}$, $\mathcal{B}$, $\mathcal{B}'$ and $\mathcal{J}$ are inhomogeneities, and $\mathcal{L}_k^{\Gamma_W}$ is the damped Mathieu differential operator with $\Gamma = \Gamma_W$. By (5.3)–(5.4), the map for the wave amplitude derivatives is the same as that for the wave amplitudes themselves. Hence, all terms in $\mathcal{B}$ of the form $a(0; k)$ are replaced by $a'(0^+; k)$ in $\mathcal{B}'$, so for notational efficiency, we do not state $\mathcal{B}'$ explicitly.

First, we note that for $\delta x = 0$, we have a bouncer at the walking threshold, so the wave field is radially symmetric, giving $a_m^{(0)} \equiv 0$ for $m \geqslant 1$. This is verified by noting that $\mathcal{H}_m^{(0)} = \mathcal{B}_m^{(0)} = \mathcal{J}_m^{(0)} = 0$ for all $m \geqslant 1$, as the only order-1 term in the Bessel expansions is in J_0. This yields a periodic unexcited solution to the damped Mathieu equation, which must be the zero solution.

To find Γ_W, we first note that $a_0^{(0)}$ and $a_1^{(1)}$ are governed by inhomogeneities

$$\mathcal{H}_0^{(0)} = 0, \quad \mathcal{B}_0^{(0)} = 0, \quad \mathcal{J}_0^{(0)} = -P_0(k), \tag{5.16a-c}$$

$$\mathcal{H}_1^{(1)} = 0, \quad \mathcal{B}_1^{(1)} = k a_0^{(0)}(0; k), \quad \mathcal{J}_1^{(1)} = -P_1(k)\,(k/2). \tag{5.17a-c}$$

Equating δx from the walking condition (5.9), we require Γ_W such that

$$1 = \frac{-\tilde{v}_p^{-1}(1 - e^{-\tilde{v}_p})}{1 - e^{-\tilde{v}_p}(1 - F(c))} \frac{F(c)}{c} \sqrt{\frac{B}{R}} \int_0^\infty \frac{k^2}{2} a_1^{(1)}(0; k)\,\mathrm{d}k. \tag{5.18}$$

Therefore, (5.16)–(5.18) is a closed system for $a_0^{(0)}$, $a_1^{(1)}$ and Γ_W. This nonlinear analysis gives a consistent walking threshold Γ_W to the linear stability analysis in §§ 4.1 and 5.1.

Given the solution to the above system, we may obtain equations for Γ_1, which is coupled with equations for $a_0^{(1)}$ and $a_1^{(2)}$. By vanishing inhomogeneities, $a_2^{(1)} \equiv 0$, so

$$\mathcal{H}_0^{(1)} = \Gamma_1 \omega_g^2(k) \cos(4\pi t + \beta) a_0^{(0)}(t; k), \quad \mathcal{B}_0^{(1)} = 0, \quad \mathcal{J}_0^{(1)} = 0, \tag{5.19a-c}$$

$$\mathcal{H}_1^{(2)} = \Gamma_1 \omega_g^2(k) \cos(4\pi t + \beta) a_1^{(1)}(t; k), \quad \mathcal{B}_1^{(2)} = k a_0^{(1)}(0; k), \quad \mathcal{J}_1^{(2)} = 0. \tag{5.20a-c}$$

The δx^2 term from (5.9) completes the system with

$$0 = \int_0^\infty \frac{k^2}{2} a_1^{(2)}(0; k)\,\mathrm{d}k. \tag{5.21}$$

We now exploit the directional symmetry of the steady walker to show that $\Gamma_1 = 0$. The map (5.1)–(5.2) also holds for $\delta x < 0$, which corresponds to a droplet walking in the negative x-direction. Since a_0 is the coefficient of the radially symmetric $J_0(kr)$ basis function, a_0 must be even in δx for the wave field to be the same for both walking directions. Hence, we require $a_0^{(1)} \equiv 0$ on $(0, 1)$. By (5.19), this is achieved if and only if $\Gamma_1 = 0$. With these vanishing terms, equation (5.20) becomes

$$\mathcal{H}_1^{(2)} = 0, \quad \mathcal{B}_1^{(2)} = 0, \quad \mathcal{J}_1^{(2)} = 0, \tag{5.22a-c}$$

yielding $a_1^{(2)} \equiv 0$ on $(0, 1)$, which satisfies (5.21). Neglecting terms of $o(\delta x^2)$, we have

$$\delta x = \Gamma_2^{-1/2} \sqrt{\Gamma - \Gamma_W}, \tag{5.23}$$

which is valid for $0 < \delta x \ll 1$. Equations for determining $\Gamma_2 > 0$ are given in appendix C. The solution is shown in figure 1(*a*) (grey curve).

5.3. *Wave field of a single impact*

Previous models for the wave field have superposed given radially symmetric sources centred at each impact with exponential temporal decay (Fort *et al.* 2010; Eddi *et al.* 2011; Moláček & Bush 2013*b*; Oza *et al.* 2013). In our model, the jump conditions (3.25)–(3.26) at time t_n are in fact equivalent to $[\eta(\boldsymbol{x}, t_n)]_-^+ = \bar{\eta}(|\boldsymbol{x} - \boldsymbol{X}(t_n)|, 0)$, where

$$\bar{\eta}(r, t) = \int_0^\infty k \bar{a}(t; k) \mathrm{J}_0(kr) \, \mathrm{d}k. \tag{5.24}$$

For all $k \geqslant 0$, $\bar{a}(t; k)$ is governed by $\mathcal{L}_k \bar{a} = 0$ for $t > 0$, with initial conditions

$$\bar{a}(0; k) = 0, \quad \bar{a}'(0; k) = -P_0(k), \tag{5.25a,b}$$

with $P_0(k) = kMG/(2\pi)$. This is quickly verified using Graf's addition theorem (Abramowitz & Stegun 1964). As $\bar{\eta}(r, 0) = 0$ for all r, the wave field is continuous across the droplet impact, which is not true in the aforementioned models. Although $\bar{\eta}_t(r, 0) = \infty$ for all $r \geqslant 0$ (from the $\delta(\cdot)$-function forcing), the rapid temporal decay of $\bar{a}(t; k)$ for large k gives a finite solution for any $t > 0$. Furthermore, $\bar{\eta}$ depends only on the current position of the droplet and is independent of its velocity and path memory.

The development of this wave field over time is shown in figure 2(*a*). A decaying capillary wave propagates away from the droplet, which excites a field of standing Faraday waves. The wave field generated is similar to that of Milewski *et al.* (2015) near the origin, but differs slightly at the wave front over time. This dissimilarity may be explained partially by the assumption of instantaneous point impacts and the truncation of the wavenumbers. As the wave speed is much larger than the walking speed, this difference has a negligible effect on the resulting dynamics.

By superposition of such wave fields, we may now express the wave field η by

$$\eta(\boldsymbol{x}, t) = \sum_{n=0}^{\lfloor t \rfloor} \bar{\eta}(|\boldsymbol{x} - \boldsymbol{X}(t_n)|, t - t_n) H(t - t_n), \tag{5.26}$$

where $H(\cdot)$ is the Heaviside function. Following Moláček & Bush (2013*b*), we define the dimensionless memory $M_e(\Gamma)$, which is the number of impacts until $\bar{\eta}$ becomes exponentially small. Using the calculations of Milewski *et al.* (2015), for $0 < \Gamma_F - \Gamma \ll 1$,

$$M_e(\Gamma) = \frac{T_d(\Gamma)}{1 - \Gamma/\Gamma_F}, \quad \text{where } T_d(\Gamma) = \frac{16\epsilon(\omega^2(k_c(\Gamma)) + \gamma^2(k_c(\Gamma)) + 4\pi^2)}{G^2 \Gamma_F^2}, \tag{5.27}$$

is the dimensionless decay rate of the waves ($\Gamma_F = 5.13$ for this fluid model). The critical wavenumber $k_c(\Gamma)$ is the least-damped wavenumber given Γ. This dependence is weak, with a 1 % variation in $k_c(\Gamma)$ away from $k_c(\Gamma_F) = k_F$ for a range of Γ,
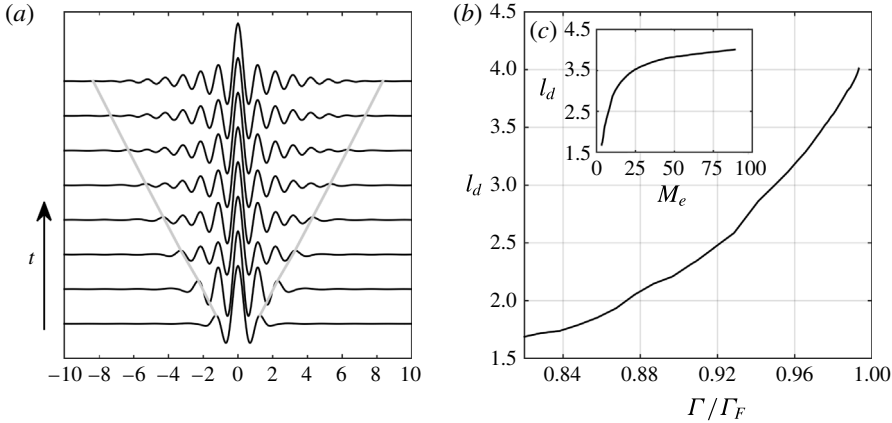
FIGURE 2. (*a*) The wave field of a single impact at times $1, \ldots, 8$, which are normalised to have the same amplitude at the origin. A damped travelling capillary wave propagates from the impact, exciting a standing field of Faraday waves in its wake ($\Gamma/\Gamma_F = 0.994$). (*b*) Spatial decay length l_d of a walker as a function of Γ/Γ_F and memory M_e (inset (*c*)).

resulting in a small variation to $T_d(\Gamma)$ (typically $T_d(\Gamma) \approx 0.6$). This form is slightly more sophisticated than that of Moláček & Bush (2013*b*), where T_d is assumed to be constant. From numerical verification, this is also a reasonable approximation for the range of Γ considered.

From figure 2(*a*), the wave field approaches a Bessel-like function as time increases. As k_F is the least-damped wavenumber, $\bar{a}(t; k)$ is peaked about $k = k_F$ for large t. Hence, the integral for $\bar{\eta}(r, t)$ may be approximated by $\bar{\eta}(r, t) = a_0(t; k_F)J_0(k_F r)$ for large t. The function $a_0(t; k_F)$ has a Floquet exponent with real part $-1/M_e$, where the underlying periodic behaviour is well approximated by a sinusoid. This long-time approximation is used by Moláček & Bush (2013*b*) and Oza *et al.* (2013), and prevents the occurrence of a travelling capillary wave formed at each impact and a Doppler shift. As our model generates a similar wave field to that of Milewski *et al.* (2015), we refer the reader to their paper for a comprehensive comparison between wave field models.

The wavenumbers near to k_F also prove to be significant in leading to the experimentally observed spatial damping (Eddi *et al.* 2011), and are computed numerically Milewski *et al.* (2015). We repeat their statistical calculation for our model, with the resulting exponential decay length l_d shown in figure 2(*b*). Specifically, we compute the wave field η for a walker, and find the extrema to $|\eta|$ in the direction perpendicular to travel. As the far-field spatial decay of a Bessel function is $\sim 1/\sqrt{r}$, we fit a nonlinear model of the form $\theta_1 \exp(-r/\theta_2)/\sqrt{r}$ for parameters (θ_1, θ_2), where $l_d = \theta_2$, which is an approximate envelope for the wave field. Typically, we consider $r \in (0, 10]$, which gives enough points for a reasonable statistical fit. As this approach contains some numerical error, the resulting solution is not smooth.

The spatial decay length l_d increases with Γ, and grows linearly with memory as $M_e \to \infty$. However, due to the fixed impact phase, we do not obtain jumps in the decay length as the impacts switch between (m, n) modes (Milewski *et al.* 2015). As Eddi *et al.* (2011) and Borghesi *et al.* (2014) used fixed dimensionless values of $l_d = 1.6$ and 2.5 respectively, they did not capture this intrinsic change in the wave field as Γ varies.
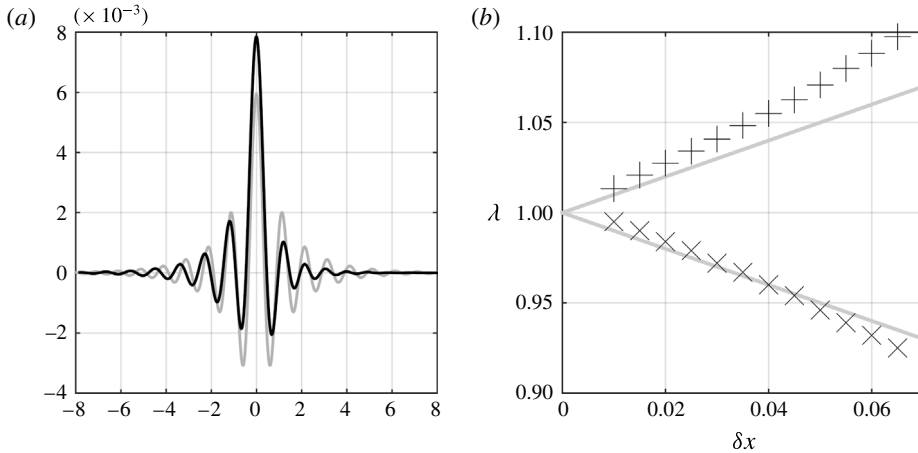
FIGURE 3. Evidence of a Doppler effect. (*a*) Wave in direction of travel (black) and transverse wave (grey) recentred to have the same peaks. The arrow determines the direction of travel, where $\Gamma/\Gamma_F = 0.9$. Waves are elongated behind the droplet and compressed ahead. (*b*) Measured wavelengths behind ($+$) and ahead ($\times$) of the droplet. The grey lines are the theoretical predictions made by Eddi *et al.* (2011).

5.4. *Doppler effect*

As shown by Eddi *et al.* (2011), a Doppler effect is observed in the wave field of the walker; the waves ahead of the droplet are compressed, yet are elongated behind. This phenomenon was observed in the simulations of Milewski *et al.* (2015). Moreover, the authors proved that this cannot occur for wave amplitudes of the form $a(t; k) = \alpha(t)\delta(k - k_F)$, which was used in Oza *et al.* (2013). However, as we maintain a significant range of k in our numerical solution, we observe a Doppler effect far from the droplet (figure 3). Our model exhibits a smooth yet nonlinear change in the wavelength due to the Doppler effect, which differs from the linear prediction of Eddi *et al.* (2011).

5.5. *Summary of steady walking dynamics*

To conclude this section, a bouncing droplet destabilises via a pitchfork bifurcation to a steady walker, whose lower-energy wave field automatically captures the exponential spatial damping correction observed in experiments (Eddi *et al.* 2011). The jump conditions are equivalent to adding a radially symmetric propagating wave field $\bar{\eta}$ at each impact, whose temporal equidistant superposition yields a Doppler shift, with a weakly nonlinear dependence on δx. Furthermore, the temporal decay of the system may be described by its memory $M_e(\Gamma)$, which allows for comparison between previous models (Fort *et al.* 2010; Moláček & Bush 2013*b*). The wave fields corresponding to the dynamics of a walker are easily computed and are shown in figures 4(*a*) and 4(*b*) for two different walking speeds. For large Γ, an interference pattern forms behind the droplet (Eddi *et al.* 2011).

6. Multiple-droplet interactions

In this section, we analyse three experimentally observed configurations for multiple droplets: orbiting pairs, side-by-side walkers (promenades) and trains of walkers. For N droplets $\boldsymbol{X}^{(1)}(t), \dots, \boldsymbol{X}^{(N)}(t)$, each droplet is governed by (3.24) during flight
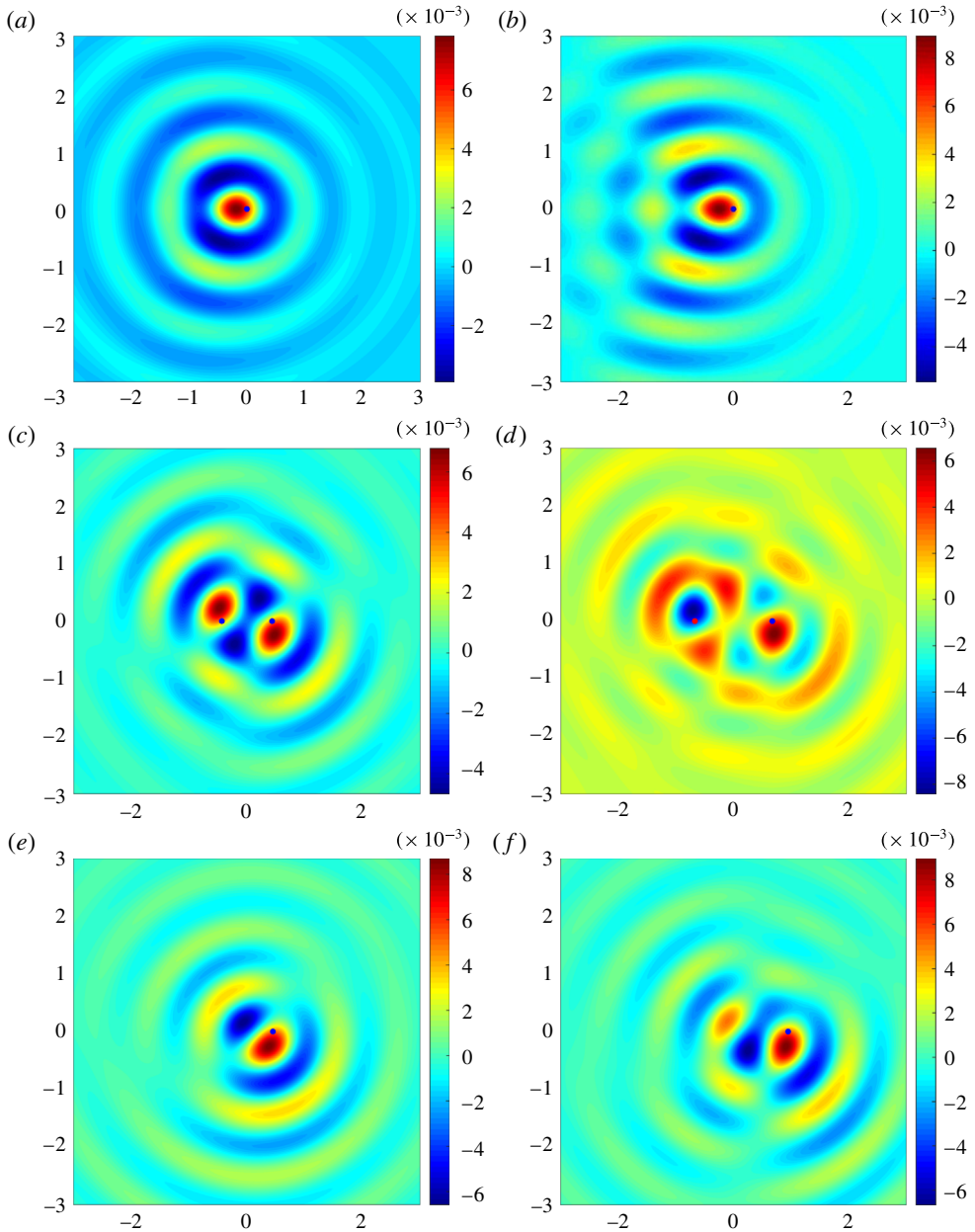
FIGURE 4. Wave fields corresponding to different steady-state dynamics at droplet impact. The droplet is denoted by a blue circle for in-phase impacts and a red circle when in flight for antiphase dynamics. Walking droplets for (*a*) $\delta x = 0.065$ with $\Gamma/\Gamma_F = 0.9$ and (*b*) $\delta x = 0.08$ with $\Gamma/\Gamma_F = 0.96$. Two anticlockwise orbiting droplets with $\Gamma/\Gamma_F = 0.91$ for (*c*) in-phase and (*d*) antiphase impacts. A single droplet orbiting anticlockwise under a central force for $\Gamma/\Gamma_F = 0.975$ with orbit radius (*e*) $R_d = 0.45$ and (*f*) $R_d = 0.95$.

(with $\tilde{\kappa} = 0$) and the jump condition (3.27) at impact. The wave amplitudes are still modelled by the damped Mathieu equations (3.22)–(3.23) during flight, but for

Stability type	Line	Description
Stable	Solid black	$\mathcal{U} = \emptyset$
Unstable (real)	Dashed black	$\mathcal{U} \cap \mathbb{R} \neq \emptyset$
Unstable (c.c.)	Solid grey	$\forall \mu \in \mathcal{U}, \ \mu \in \mathbb{C} \backslash \mathbb{R}$ and $\bar{\mu} \in \mathcal{U}$

TABLE 2. Stability types of the stability transition matrix $\boldsymbol{T}$ with complex eigenvalue spectrum $\sigma(\boldsymbol{T})$. We define the set of unstable eigenvalues $\mathcal{U} = \{\mu : \mu \in \sigma(\boldsymbol{T}), \ |\mu| > 1\}$, where $\mathcal{U}$ is empty only when the system is stable.

in-phase interactions, the jump condition (3.25) becomes

$$[a_m'(t_n; k)]_-^+ = -P_m(k) \sum_{p=1}^{N} \Phi_m(X^{(p)}(t_n); k), \tag{6.1}$$

and similarly for b_m'. For antiphase impacts, additional jumps occur at $t = t_{n+1/2} \equiv t_n + 1/2$. In the bifurcation diagrams that follow in §§ 6 and 7, we identify three stability types, as described in table 2. A pair of unstable complex conjugate (c.c.) eigenvalues often allows the system to destabilise slowly to a new oscillatory stable regime.

6.1. *In-phase orbiting*

We consider two orbiting droplets about the origin; both droplets impact simultaneously on a radius R_d, with the droplets and wave field rotating by an angle $\delta\theta > 0$ between impacts. Moreover, we pose that the angular difference between $X^{(1)}(t_n)$ and $X^{(2)}(t_n)$ is π for all t_n. This allows us to model $X^{(1)}(t)$ explicitly, with the contribution of $X^{(2)}(t_n)$ to the wave amplitude jump conditions treated implicitly. For notational convenience, we write $X(t) \equiv X^{(1)}(t)$, where $X(t_n)$ has radial component $r_d(t_n) = R_d$ and angular component $\theta_d(t_n) = \theta_n \equiv n\delta\theta$ (by rotational invariance). The droplet motion is piecewise linear, so $r_d(t) \neq R_d$ for $t \neq t_n$.

As the implicit second droplet has angular component $(\theta_n + \pi)$ at time t_n, (6.1) gives

$$[a_m'(t_n; k)]_-^+ = -P_m(k) \Phi_m(X(t_n); k)(1 + (-1)^m), \tag{6.2}$$

$$[b_m'(t_n; k)]_-^+ = -P_m(k) \Psi_m(X(t_n); k)(1 + (-1)^m). \tag{6.3}$$

For m odd, a_m and b_m are never excited during the orbit, giving $a_m \equiv b_m \equiv 0$. This ensures that the wave field with respect to each droplet is the same.

Denoting $\boldsymbol{c}_m(t; k) = (a_m(t; k), b_m(t; k))^{\mathrm{T}}$, the wave field rotates with the droplets if

$$\boldsymbol{c}_m(t_{n+1}; k) = \boldsymbol{D}(m\delta\theta)\boldsymbol{c}_m(t_n; k), \quad \boldsymbol{c}_m'(t_{n+1}^+; k) = \boldsymbol{D}(m\delta\theta)\boldsymbol{c}_m'(t_n^+; k), \tag{6.4a,b}$$

where $\boldsymbol{D}(\varphi) \in \mathbb{R}^{2\times 2}$ is the rotation matrix for angle φ. The droplet rotation requires

$$X(t_{n+1}) = \boldsymbol{D}(\delta\theta)X(t_n), \quad X'(t_{n+1}^+) = \boldsymbol{D}(\delta\theta)X'(t_n^+). \tag{6.5a,b}$$

As with steady walking, we solve the droplet dynamics (3.24)–(3.27) with $\tilde{\kappa} = 0$ for $t \in [t_n, t_{n+1})$ subject to (6.5), and eliminate $X'(t_n^+)$ in favour of $X(t_n)$. This gives

$$(\boldsymbol{D}(\delta\theta) - (1 - F(c))e^{-\tilde{v}_p}\boldsymbol{I}_2)(\boldsymbol{D}(\delta\theta) - \boldsymbol{I}_2)X(t_n) = \frac{-F(c)}{c}\frac{1 - e^{-\tilde{v}_p}}{\tilde{v}_p}\sqrt{\frac{B}{R}}\boldsymbol{D}(\delta\theta)(\nabla\eta)_n, \tag{6.6}$$

where $(\nabla\eta)_n \equiv \nabla\eta(X(t_n), t_n)$, and $(\nabla\eta)_{n+1} = \boldsymbol{D}(\delta\theta)(\nabla\eta)_n$ due to the rotation.
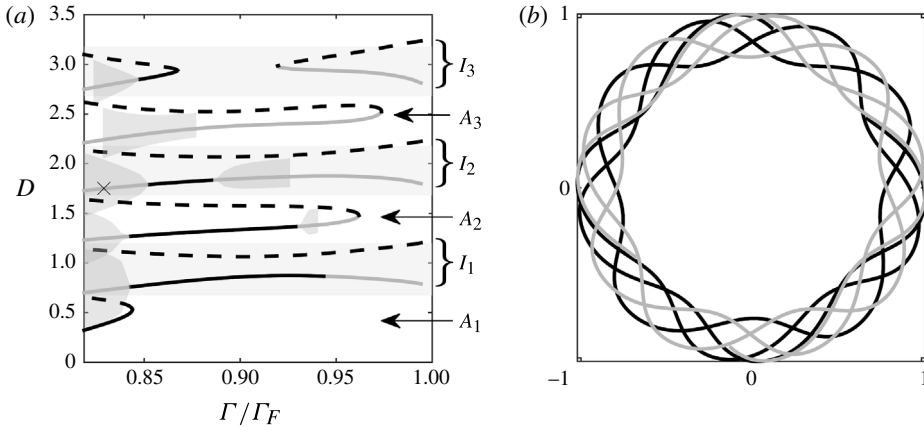
FIGURE 5. (*a*) Bifurcation diagram for the diameters D of in-phase I_n (light grey background) and antiphase A_n (white background) orbiting pairs. The dark grey regions give the bounds for two droplets in a stable wobbly orbit. This has an upper bound given by the unstable upper branch. The curves correspond to stability types in table 2. (*b*) Example wobbly in-phase anticlockwise orbiters with $\Gamma/\Gamma_F = 0.83$, which corresponds to the black cross in (*a*).

We need to find R_d and $\delta\theta$ such that the wave field amplitudes governed by (3.22)–(3.23) with jump conditions (6.2)–(6.3) satisfy the rotation conditions (6.4) and droplet condition (6.6). By periodicity, it is sufficient to solve for $n = 0$ (so $t \in [0, 1]$), where $X(t_0) = (R_d, 0)^T$. This is formulated as many 4×4 linear systems subject to (6.6), akin to finding the walking states. An example in-phase wave field is given in figure 4(*c*).

The stability analysis is similar to that of the walking states with two independent droplet perturbations, although we rotate the domain by $\delta\theta$ between iterations so that the steady-state droplet always lies at $(r, \theta) = (R_d, 0)$ in the current domain. It should be noted that the wave amplitudes a_m and b_m are required for all m (not just even indices), and the system is truncated for sufficiently large m given R_d, by the shape of the large-order Bessel functions near zero (it should be recalled that $J_m(z) \sim (1/m!)(z/2)^m$ for $0 < z \ll \sqrt{m+1}$).

The orbit diameters $D \equiv 2R_d$ are shown in figure 5(*a*), where curves with a light grey background correspond to in-phase orbiters. The diameters of the stable solutions are in good agreement with the experimental values recorded by Couder *et al.* (2005*b*), namely $D_n = (n - \bar{\epsilon})$, where $\bar{\epsilon} \approx 0.2$ and n is an integer. However, the co-existence of stable $n = 1, 2, 3$ orbits occurs only for a limited range of Γ. This system also contains wobbly orbits, which appear when the steady orbit destabilises via a complex conjugate pair of eigenvalues. Due to nonlinear effects, the droplets remain locked in a periodic wobbly orbit (see figure 5(*b*)). The minimum and maximum distances apart reached by the droplets are indicated by the dark grey regions in figure 5(*a*), and are obtained by simulating away from the steady states. We observe that the maximum distance apart is bounded above by the corresponding unstable upper branch to each solution, which sheds some light on why wobbly solutions only exist over a limited range of Γ.

For further insight, we consider the solution at $\Gamma = \Gamma_F$ with wavenumber $k = k_F$. The Floquet exponents are $\mu_1 = 0$ and $\mu_2 = -2\gamma(k_F)$, giving the eigenvalues of the Mathieu fundamental matrix $\boldsymbol{M}_{k_F}(\Gamma_F)$ as $\rho_1 \equiv \exp(\mu_1) = 1$ and $\rho_2 \equiv \exp(\mu_2)$. Periodicity

requires

$$(I_2 - M_{k_F}(\Gamma_F)) \begin{pmatrix} a_0(0; k_F) \\ a_0'(0; k_F) \end{pmatrix} = - \begin{pmatrix} 0 \\ 2P_0(k_F)J_0(k_F R_d) \end{pmatrix}, \qquad (6.7)$$

where $(I_2 - M_{k_F}(\Gamma_F))$ is singular. A candidate radius R_d satisfies $J_0(k_F R_d) = 0$, with a corresponding wave amplitude vector from the matrix null space. In fact, such radii satisfy the full problem and correspond to the lower branches in figure 5(a) as $\Gamma \to \Gamma_F$.

6.2. *Antiphase orbiting*

For antiphase orbiting of two droplets, we impose that $X^{(1)}(t_n)$ and $X^{(2)}(t_{n+1/2})$ both lie on the radius R_d with angular components θ_n and $(\theta_{n+1/2} + \pi)$ respectively, where $t_{n+1/2} \equiv t_n + 1/2$ and $\theta_{n+1/2} \equiv \theta_n + \delta\theta/2$. We construct the wave field to rotate by $\pi + \delta\theta/2$ in half of an impact period, which ensures that the wave field is the same with respect to each droplet at impact. The antiphase jump conditions are

$$[a_m'(t_{n+1/2}; k)]_-^+ = -P_m(k)(-1)^m \Phi_m(R_d, \theta_{n+1/2}; k), \qquad (6.8)$$

$$[b_m'(t_{n+1/2}; k)]_-^+ = -P_m(k)(-1)^m \Psi_m(R_d, \theta_{n+1/2}; k). \qquad (6.9)$$

Hence, both odd and even m are required for antiphase orbiters.

It remains to find R_d and $\delta\theta$ such that (6.6) is satisfied. This is coupled with Mathieu equations (3.22)–(3.23), jump conditions (6.8)–(6.9) and wave amplitude maps (6.4), but with $t_{n+1} \mapsto t_{n+1/2}$ and $\delta\theta \mapsto \pi + \delta\theta/2$. An example wave field is shown in figure 4(d). The stability analysis requires a two-stage transition map to account for the antiphase impacts.

The quantisation of antiphase orbiters is given by the regions of white background shown in figure 5(a). Although the reported orbit quantisation $D_n' = (n + 1/2 - \bar{\epsilon})$ is obtained (Couder *et al.* 2005b), the range of stable solutions with Γ is limited, particularly for the smallest orbit. We note that the stability and existence of solutions are dependent on the skidding friction c and impact phase β, which are both fixed for this theoretical investigation. We expect that these results will be particularly sensitive to the impact phase.

6.3. *Promenade pairs*

For simplicity, we only analyse rectilinear promenade pairs. To exploit the symmetry of two in-phase droplets, we fix the droplets to walk in parallel along lines $y = \pm\delta y$ in the direction of increasing x. To find δy, we require $\partial_y \eta = 0$ at each drop, and the walking speed δx is given by an equation analogous to (5.9). This couples with the wave amplitude maps (5.3)–(5.4) and multiple-droplet jump conditions (6.1), with $X^{(1)}(t_n) = (n\delta x, \delta y)$ and $X^{(2)}(t_n) = (n\delta x, -\delta y)$. The stability analysis follows similarly to the walking case, yet the two droplets have independent perturbations.

The extension to antiphase promenaders is analogous to that for orbiters. In half of an impact period, we require the wave field to be translated $\delta x/2$ along the x-axis and reflected about $y = 0$. This ensures that each droplet receives the same *kick* at impact.

Results are shown in figure 6(a), where the grey and white backgrounds correspond to in-phase and antiphase dynamics, respectively. We first observe that the speed of a promenading pair is less than that of a single walker, as reported by Borghesi *et al.* (2014). The quantised distance between droplets $D \equiv 2\delta y$ depends weakly on Γ, which was not reported in Borghesi *et al.* (2014). Instead, the authors stated
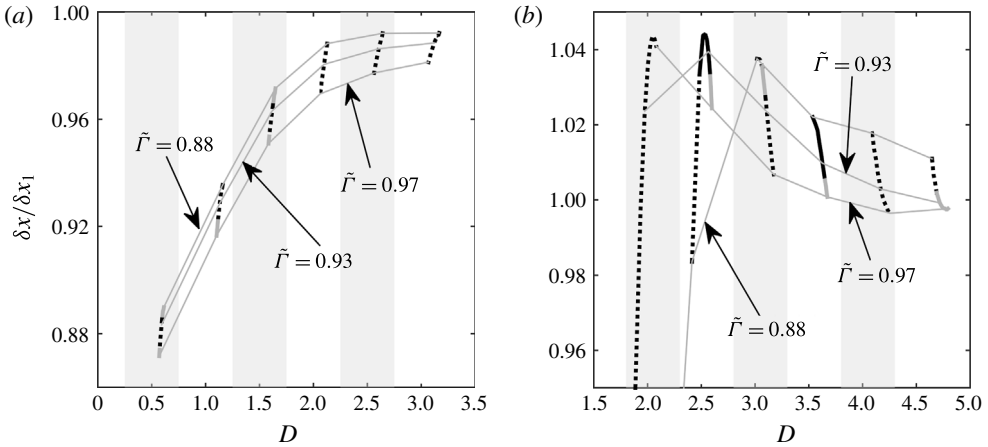
FIGURE 6. Bifurcation diagram for (*a*) promenade pairs and (*b*) two-droplet trains as a function of distance apart D and speed relative to a single walker $\delta x/\delta x_1$. Grey and white backgrounds denote in-phase and antiphase dynamics respectively. The thin grey lines connect points of equal $\tilde{\Gamma} \equiv \Gamma/\Gamma_F$. The thick lines correspond to stability types in table 2.

that D has approximate in-phase values of $0.6, 1.6, 2.6, \ldots$ and antiphase values of $1.1, 2.1, 3.1, \ldots$, which is consistent with our findings.

Crucially, we note that straight-line promenade pairs are unstable for all quantisations and all values of Γ. When there is an oscillatory instability (with no real eigenvalue), we expect the droplets to become bound in parallel motion, but with a transverse oscillation, as reported in experiments (Protière *et al.* 2006; Borghesi *et al.* 2014). This is demonstrated in figure 7, where we simulate from the unstable steady state (with no real unstable eigenvalues), and nonlinear effects keep the droplets in a steady oscillatory bound state. Such a result was speculated on by Borghesi *et al.* (2014), but is hard to observe experimentally due to the confines of a finite domain. The size of these oscillations depends on the skidding friction c and phase shift β free parameters, which would both be tuned for a more careful comparison with experimental data. Larger c increases the solution space for oscillatory pairs, and the transverse extent of the oscillations is reduced.

To shed light on the instability of straight-line promenaders, we construct a new wave field based on the superposition of two parallel walkers (from § 5), and compare the average wave field energy over one impact period (appendix B). The distance between each walker is given by the continuous parameter D. The antiphase case requires a mid-period impact for the second droplet; this presents a minor difficulty as we do not know the speed of the newly constructed walking pair, so the impact location is unknown (it should be recalled that a promenading pair travels slower than a single walker). For ease, we assume that the pair of walkers travel at the same speed as a single walker, which determines the impact location. We note that any error for this impact is small, and as the energy is a quadratic function of the wave amplitudes, this gives a negligible change to the energy.

Results of this calculation are shown in figure 8. Intuitively, we expect the energy of the walking pair to be minimised at the same distance as that of the promenading pair. However, the walking pair do not obey the condition $\partial_y \eta = 0$ at each droplet,
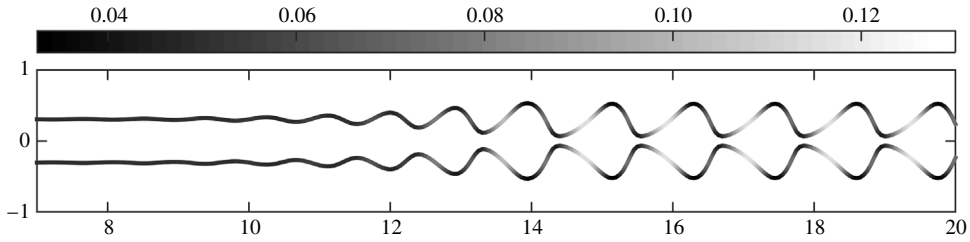
FIGURE 7. Example transition from an unstable straight-line promenade (starting at $x = 0$) to a stable oscillating promenade, with the speed given by the grey scale bar.
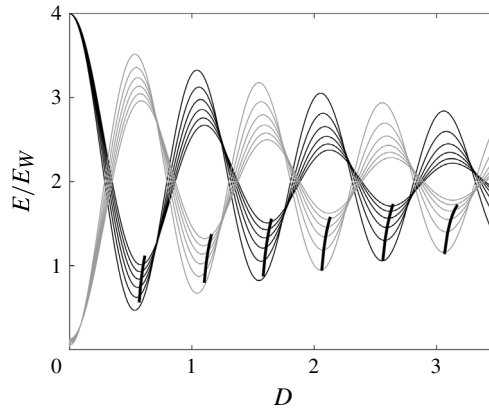

FIGURE 8. Wave field energy E/E_W (relative to a single walker) for two in-phase (black) and antiphase (grey) parallel walkers at a distance D apart for different values of Γ. The larger values of Γ give the most extreme variations in energy ($\Gamma/\Gamma_F = 0.88, 0.9, \ldots, 0.98$). The thick black lines give the energy of the corresponding quantised parallel promenade solutions. The required interaction energy for the promenade mode partially explains its instability.

which is required for a parallel procession. Hence, additional energy must be stored in the wave field in the case of the quantised promenaders, whose energy range (with Γ) is denoted by the thick black lines in figure 8. The difference in energy decreases as D increases due to the spatial decay of the wave field of the walker. Physically, the wave field would tend to adopt the lowest-energy state of two walkers; however, as this motion cannot be rectilinear (since $\partial_y \eta \neq 0$ at each droplet impact), a transverse oscillation ensues.

6.4. *Droplet trains*

Trains of droplets may be studied in a similar fashion to promenades, except that all droplets lie on the x-axis and are spaced δs apart. This requires constant $\partial_x \eta$ at each droplet, with the in-phase and antiphase results shown in figure 6(b), where we denote $D \equiv \delta s$. For sufficiently large Γ, two droplets may walk faster than a single droplet, which was also observed for experiments in a confined annulus (Filoux, Hubert & Vandewalle 2015). The stability types reported in figure 6(b) are for general perturbations, although the droplet trains are neutrally stable in the direction of travel

(like a single walking droplet). Interestingly, the presence of a second droplet stabilises the system to general perturbations for some antiphase trains. A possible extension is to consider trains of multiple droplets, as considered in an annulus by Filoux *et al.* (2015).

7. Droplet dynamics under a central force

When a droplet is subjected to a central force ($\tilde{\kappa} > 0$ in (3.24)), a range of new dynamics occur. For increasing Γ, a bouncing droplet may destabilise to a circular orbit, which itself destabilises to a variety of trajectories whose average radius and angular momentum are quantised (Perrard *et al.* 2014*b*). Analysis for circular orbits is analogous to § 6.1, but the more complex dynamics are explored numerically.

7.1. *Circular orbits*

For a single droplet in a circular orbit, the wave amplitudes must satisfy the rotational maps (6.4*a*,*b*), and are governed by (3.22)–(3.23) with jump conditions (3.25)–(3.26). However, as $\tilde{\kappa} > 0$, the droplet rotation condition (6.6) becomes

$$F(c) \left(\frac{\mu_+ \mathrm{e}^{\mu_+} - \mu_- \mathrm{e}^{\mu_-}}{\mu_+ - \mu_-} \boldsymbol{D}(\delta\theta) - \mathrm{e}^{-\tilde{\nu}_p} \boldsymbol{I}_2 \right) \boldsymbol{X}(t_n) + (\boldsymbol{D}(\delta\theta) - \mathrm{e}^{\mu_+} \boldsymbol{I}_2)(\boldsymbol{D}(\delta\theta) - \mathrm{e}^{\mu_-} \boldsymbol{I}_2)\boldsymbol{X}(t_n)$$
$$= \frac{-F(c)}{c} \sqrt{\frac{B}{R}} \left(\frac{\mathrm{e}^{\mu_+} - \mathrm{e}^{\mu_-}}{\mu_+ - \mu_-} \right) \boldsymbol{D}(\delta\theta)(\nabla\eta)_n, \tag{7.1}$$

where

$$\mu_\pm \equiv \tfrac{1}{2}(-\tilde{\nu}_p \pm \sqrt{\tilde{\nu}_p^2 - 4\tilde{\kappa}}). \tag{7.2}$$

When $\mu_\pm \in \mathbb{C}$, we use Euler's formula to ensure a real solution, whose stability is analysed analogously to § 6.1. Example wave fields are given in figure 4(*e*,*f*).

We characterise this system with $\Lambda(\Gamma) \equiv \delta x(\Gamma)/\sqrt{\tilde{\kappa}}$, where $\delta x(\Gamma)$ is the steady walking speed for $\tilde{\kappa} = 0$. For a classical orbit, balancing the spring constant $\tilde{\kappa}$ and centripetal acceleration gives the orbit radius $R_d = \Lambda$. However, the droplet interaction with the wave field leads to a more complicated radius structure as Γ increases (figure 9), where the unstable orbits require a larger average wave field energy. As with the in-phase orbiters, radii R_d satisfying $J_0(k_F R_d) = 0$ are solutions when $\Gamma = \Gamma_F$, which approximately correspond to the upper plateaus in figure 9(*b*). Noting that $\Lambda = \infty$ corresponds to $\tilde{\kappa} = 0$, figure 9(*b*) suggests that orbital solutions in the absence of a central force are possible for sufficiently high Γ. In the present parameter regime, self-orbiters are not stable; simulation from the self-orbiter initial conditions ($R_d \approx 0.42$) yields only two complete orbits at $\Gamma/\Gamma_F = 0.994$ before the trajectory diverges.

When the circular orbits destabilise, a range of new orbits appear, with common examples shown in figure 10. In § 7.2, we see how these orbits manifest themselves at even larger Γ, where all orbits are unstable.

7.2. *Towards a double quantisation*

As shown in the experiments of Perrard *et al.* (2014*b*), these exotic orbits exhibit a double quantisation in their mean radius and angular momentum in their stable states. The quantised states follow the same selection rule as the energy and angular momentum of a quantum particle in a two-dimensional potential well. Specifically,
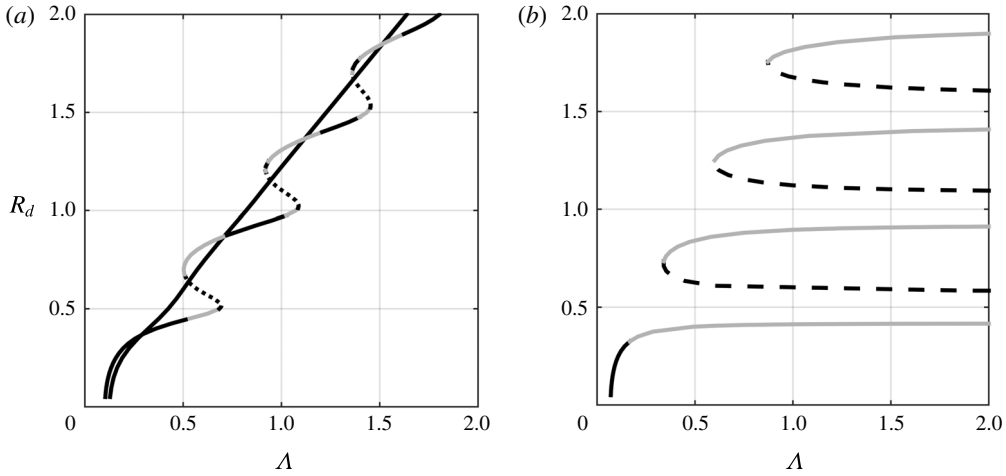
FIGURE 9. Bifurcation diagram for orbit radius R_d of a droplet in a harmonic potential well of width Λ. In (*a*), $\Gamma/\Gamma_F = 0.916$ (almost linear) and $\Gamma/\Gamma_F = 0.975$ (snaked curve). In (*b*), $\Gamma/\Gamma_F = 0.994$. The lines correspond to stability types in table 2.
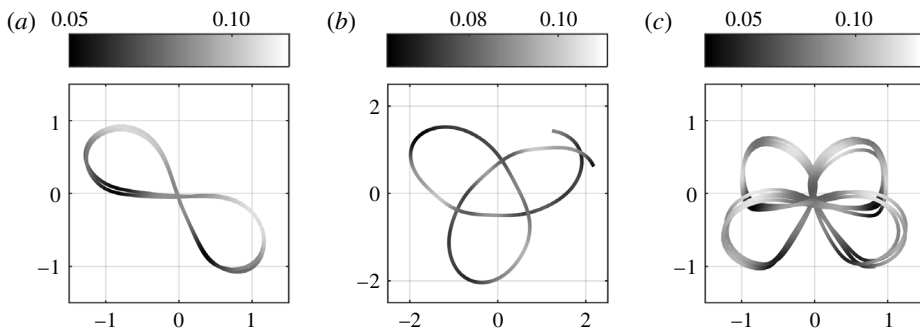

FIGURE 10. Example trajectories (lemniscate, trefoil and butterfly) for $\Gamma/\Gamma_F \approx 0.975$ and different values of Λ. The colour bars indicate the speed of the droplet.

the radius and angular momentum form a (p, q) lattice, where p is an integer and $q \in \{-p, -p+2, \ldots, p-2, p\}$. These points correspond to the grey crosses ($\times$) in figures 11 and 12.

Although we obtain a similar quantisation for stable orbits, the methods of Perrard *et al.* (2014*b*) rely on a range of Γ and Λ in an unsystematic way. Instead, we explore the dynamics in the chaotic regime for fixed Γ, whereby the observed orbits destabilise but continue to be recognisable over short time intervals. This allows for a novel and methodical analysis of the long-time dynamics, yielding a similar double quantisation.

For a given circular orbit radius $R_d > 0$, there exist unique $\delta\theta > 0$, $\Lambda > 0$ and the corresponding wave field (see the example in figure 9(*a*) with $\Gamma/\Gamma_F = 0.975$). This provides a well-defined systematic initial condition for numerical simulation. We simulate over $(N_0 + N)$ impacts, where the first N_0 impacts are a 'burn-in' period (omitted from further analysis). This is the time allowed for the droplet to destabilise
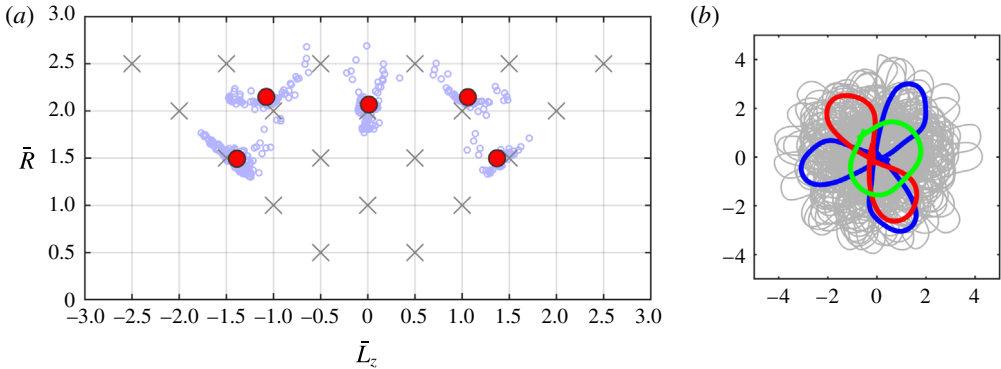
FIGURE 11. (*a*) Example clustering for a single trajectory with $\Gamma/\Gamma_F = 0.984$ and $\Lambda = 1.23$. The light blue circles are averages over sections and the grey crosses form the approximate lattice for the quantum double quantisation. The red dots are the cluster centroids for this example (initially, $R_d = 1.75$ and $\delta\theta > 0$). (*b*) The corresponding trajectory (grey) with example coloured sub-trajectories shown over short time intervals.

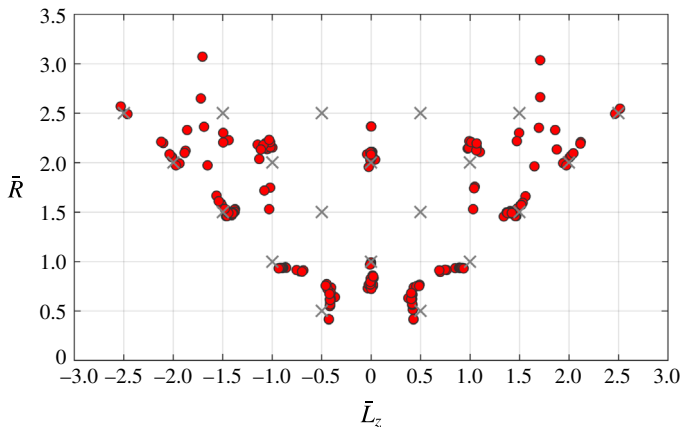

FIGURE 12. Double quantisation for a droplet in a harmonic potential for $\Gamma/\Gamma_F = 0.984$. The grey crosses form the quantum double quantisation lattice and the red dots are the cluster centroids for simulations over all initial radii $R_d \in \{0.4, 0.425, \ldots, 2\}$ and corresponding values of Λ, with both $\delta\theta > 0$ and $\delta\theta < 0$ initially.

from its circular orbit and begin to explore the underlying probability distribution of the dynamics. Throughout this work, we fix $N_0 = 3000$ impacts and $N = 3 \times 10^4$, where N_0 is estimated by considering the unstable eigenvalues of the system and N is large enough so that the resulting probability distribution is ergodic. For stable circular orbits, the droplet remains on its initial trajectory for all impacts. We perform this process for $R_d \in \{0.4, 0.425, \ldots, 2\}$, which removes the stable orbits for small Λ in which the central force dominates the trajectory. Simulation from initial conditions with $\delta\theta < 0$ does not yield a corresponding symmetric trajectory (as the dynamics are chaotic), but the statistics are unchanged.

It remains to analyse the data from these trajectories. Following Perrard *et al.* (2014*b*), we define the dimensionless mean radius $\bar{R}$ and mean angular momentum

$\bar{L}_z$ as

$$\bar{R} = \frac{1}{\sqrt{N}} \left(\sum_{n=1}^{N} r_d(t_{n+N_0})^2 \right)^{1/2}, \quad \bar{L}_z = \frac{1}{N} \sum_{n=1}^{N} \left(X(t_{n+N_0}) \times \frac{1}{\delta x(\Gamma)} X'(t_{n+N_0}^+) \right) \cdot e_z,$$

$$(7.3a,b)$$

where $r_d(t)$ is the droplet radius at time t and $\times$ denotes the vector product.

When simulating from an oscillatory instability, we expect to obtain wobbling circular orbits. However, when a real unstable eigenvalue exists, the trajectory is pushed away from the circular orbit, and more exotic dynamics occur. From the work of Perrard *et al.* (2014*b*), we expect to obtain trajectories that resemble lemniscates and trefoils on a short time scale, but appear chaotic on a long time scale (see the examples in figure 10). Although taking averages over all N impacts makes some progress towards a double quantisation, trajectories with switching states (typically between lemniscates and ovals) blur this picture. As these states are non-constant and unstable, it is difficult to identify switching times without hand-picking the data (as in Perrard *et al.* (2014*b*)), so we seek an alternative approach.

The answer lies in a further understanding of stable lemniscate and trefoil orbits. Our systematic analysis starts off by segmenting the long trajectory into shorter sections between the radial maxima of impacts. This yields well-defined cutting times. For a fictitious stable lemniscate, the mean radius and angular momentum are the same between two radial maxima compared with the whole trajectory (we have 'half' of a lemniscate). Similarly, the radial maxima break a fictitious stable trefoil into three identical sections (up to a rotation of $2\pi/3$). For a stable circular orbit, each point is defined as a radial maximum. Hence, we proceed by splitting each trajectory into intervals between radial maxima, and compute $\bar{R}$ and $\bar{L}_z$ over each interval.

For each trajectory, we may visualise the resulting interval mean data by plotting a scatter graph in the $(\bar{L}_z, \bar{R})$-plane (see the example in figure 11). Each trajectory gives rise to a well-separated set of clusters of mean radius and angular momentum points, where multiple clusters only arise in the case of switching states. This motivates cluster analysis as a suitable statistical approach to completing the double quantisation.

To calculate the clusters for each simulation, we use K-means clustering, where K is a predetermined number of clusters (Hartigan 1975; Hartigan & Wong 1979). The aim is to globally minimise the cost function, which is the total Euclidean distance between points. Each sub-trajectory is weighted by its number of impacts; this prevents smaller trajectories from being favoured (as radial maxima are achieved more frequently). The algorithm takes random initial locations for the cluster means (centroids) and is guaranteed to converge to a local minimum of the cost function. A sufficiently large number of repetitions is likely to locate the global minimum, which determines the locations of the centroids. When $K = 1$, this is simply the global mean of the data.

The issue with all clustering techniques is determining the value of K. As it happens, the cases considered for this double quantisation can almost be identified by eye; the example in figure 11(*a*) has $K = 5$ well-separated clusters. However, statistical techniques also exist as a guide for the number of clusters, such as the elbow method, silhouettes and cross-validation (Kodinariya & Makwana 2013). However, the great benefit of clustering in this application is that the technique automatically groups together similar trajectories and averages over them. The outlier trajectories (say the transitions between lemniscates and ovals) are infrequent so do not skew the data.

By combining the centroids from all of the simulations, we obtain a double quantisation in $(\bar{L}_z, \bar{R})$ in the chaotic regime ($\Gamma/\Gamma_F = 0.984$), as shown in figure 12. We note that Perrard *et al.* (2014*b*) also observed a less sharp quantisation for $\bar{R} > 2$. There is a notable dearth of centroids around (± 0.5, 1.5); the loop tractories corresponding to this quantisation are unstable and only exist for much larger values of Γ considered. The loops are the combination of straight-line solutions and spin states, whereby a single droplet may orbit itself in the absence of a central force. The existence of these unstable spin states can be seen from figure 9(*b*) for large Λ (corresponding to small $\tilde{\kappa}$). However, the centroids at approximately (± 1, 1.5) are stable trefoil-like features not reported in Perrard *et al.* (2014*b*). A more thorough investigation may lead to the discovery of new trajectories that alter the shape of the double quantisation.

8. Discussion

We have derived a new discrete-time model for the Faraday wave–droplet interactions on a vibrating bath, yielding stability analysis of fixed points, with many bifurcations explained through energy considerations. The map structure also allows us to explore the statistics of the system through extremely efficient numerical simulations. By analysing bouncing and walking states, we captured an improved wave field that exhibits a Doppler effect, exponential spatial damping and the travelling capillary wave from a single impact. These features are not present in the trajectory equation of Oza *et al.* (2013).

For two interacting droplets, we modelled orbiters, promenade pairs and droplet trains. For orbiters, we identified the experimentally observed quantisation for the orbit diameter and analysed the stability. By considering the unstable upper branch for each orbit, we obtained an upper bound for the extent of stable wobbly orbits. This gives a partial explanation for the restricted existence of these states. We also showed that straight-line promenade pairs are unstable, but for weak oscillatory instabilities it is possible to transition from straight-line promenades to promenades with transverse oscillations, as hypothesised by Borghesi *et al.* (2014). We performed the first analysis for droplet trains in an unbounded domain, and showed that in a certain parameter regime, the train travels faster than a single droplet. This feature was also observed in the annulus experiments of Filoux *et al.* (2015).

Finally, we explored the dynamics of a droplet in a harmonic potential. We studied the stability of circular orbits and obtained similar results to Labousse *et al.* (2016). By simulating in the chaotic regime and exploiting cluster analysis, we showed that the trajectories obey a double quantisation for a single value of Γ.

Despite the success of this model in a variety of situations, the dynamics are still restricted to the (2, 1) mode with prescribed impact phase. In the future, we aim to relax this restriction while maintaining instantaneous impacts to allow for mathematical analysis akin to this work. This will allow us to explore the bifurcation between a range of (m, n) impact modes, with a self-selecting impact phase. Furthermore, as we have only considered an unbounded fluid domain, we are unable to model the interaction with submerged obstacles, such as slits and barriers. Future work on this will lend far greater insight into the experimentally observed diffraction and interference patterns (Couder & Fort 2006), tunnelling (Eddi *et al.* 2009) and the droplet probability distribution in a quantum-like corral (Harris *et al.* 2013).

Acknowledgements

Appendix A. Derivation of the droplet jump condition

For ease, we generalise (3.20) to the scalar differential equation

$$u''(t) + Cu'(t)\delta(t - t_\star) = \mathcal{G}(t, u(t), u'(t)) + \mathcal{F}(t, u(t))\delta(t - t_\star), \tag{A 1}$$

where $\mathcal{F}$ is bounded and piecewise smooth except for a jump in $\partial \mathcal{F}/\partial t$ at $t = t^\star > 0$. We assume that $\mathcal{G}$ is bounded along a solution to (A 1) over the interval $(0, t)$, including at $t = t_\star$. Catllá *et al.* (2008) considered the special case $\mathcal{G} = -u'(t)$ and constant forcing $\mathcal{F}$.

We define a generalised δ-function δ_ε and corresponding Heaviside function H_ε as

$$\delta_\varepsilon(t - t_\star) = \frac{1}{\varepsilon}\varphi\left(\frac{t - t_\star}{\varepsilon}\right), \quad H_\varepsilon(t - t_\star) = \int_0^t \delta_\varepsilon(s - t_\star)\,\mathrm{d}s, \tag{A 2a,b}$$

where $\varphi(s) \geqslant 0$ for all $s \in \mathbb{R}$ and $\int_{-\infty}^{\infty} \varphi(s)\,\mathrm{d}s = 1$. We will integrate (A 1) once to give an integro-differential equation for the cases $t < t_\star$ and $t > t_\star$. By taking the limits $\varepsilon \to 0$ and $t \to t_\star^{\pm}$, we obtain the jump $[u'(t_\star)]_-^+$, which is independent of φ.

For $t < t_\star$, (A 1) simplifies to $u''(t) = \mathcal{G}$. Integrating once yields $u'(t) = u'(0) + \int_0^t \mathcal{G}$, which gives $u'(t_\star^-) = u'(0) + \int_0^{t_\star} \mathcal{G}$. For $t > t_\star$, we replace δ with δ_ε in (A 1) and use the integrating factor $\mathrm{e}^{CH_\varepsilon(t - t_\star)}$ to obtain $u'(t)\mathrm{e}^{CH_\varepsilon(t - t_\star)} = I_1(t) + I_2(t)$, where

$$I_1(t) = u'(0) + \int_0^t \mathcal{G}\mathrm{e}^{CH_\varepsilon(s - t_\star)}\,\mathrm{d}s \quad \text{and} \quad I_2(t) = \int_0^t \mathcal{F}\delta_\varepsilon(s - t_\star)\mathrm{e}^{CH_\varepsilon(s - t_\star)}\,\mathrm{d}s. \tag{A 3a,b}$$

In $I_1(t)$, the integrand is bounded almost everywhere and is integrable over $[0, t]$, so for $t < \infty$ the bounded convergence theorem gives $\lim_{\varepsilon \to 0} I_1(t) = u'(0) + \int_0^{t_\star} \mathcal{G} + \mathrm{e}^C \int_{t_\star}^t \mathcal{G}$. Hence, $I_1(t_\star^+) = u'(t_\star^-)$.

The integral for $I_2(t)$ is more delicate. To proceed, we split the integral $\int_0^t = \int_0^{t_\star - \xi} + \int_{t_\star - \xi}^{t_\star + \xi} + \int_{t_\star + \xi}^t$, for some suitable $\xi > 0$, where the two outer integrals tend to zero as $\xi \to 0$ for any $\varepsilon > 0$. This is shown by first using the boundedness of $\mathcal{F}$ and $H_\varepsilon(s) \leqslant 1$, which results in an integral over δ_ε. The final stage is to substitute in the definition of δ_ε, change variables $\tau = (s - t_\star)/\varepsilon$ and use the fact that $\varphi(\pm\infty) = 0$.

We now examine the behaviour of the integral $\int_{t_\star - \xi}^{t_\star + \xi}$ in the limit $\varepsilon \to 0$. As

$$\delta_\varepsilon(s - t_\star)\mathrm{e}^{CH_\varepsilon(s - t_\star)} = \frac{1}{C}\frac{\mathrm{d}}{\mathrm{d}s}\left(\mathrm{e}^{CH_\varepsilon(s - t_\star)}\right), \tag{A 4}$$

we integrate by parts to obtain

$$\int_{t_\star - \xi}^{t_\star + \xi} \mathcal{F}(s, u(s))\delta_\varepsilon(s - t_\star)\mathrm{e}^{CH_\varepsilon(s - t_\star)}\,\mathrm{d}s = \frac{1}{C}\left[\mathcal{F}(s, u(s))\mathrm{e}^{CH_\varepsilon(s - t_\star)}\right]_{t_\star - \xi}^{t_\star + \xi} - \frac{1}{C}Q_{\varepsilon,\xi}, \tag{A 5}$$

where

$$Q_{\varepsilon,\xi} = \int_{t_\star - \xi}^{t_\star} \frac{d\mathcal{F}}{ds} e^{CH_\varepsilon(s - t_\star)} \, ds + \int_{t_\star}^{t_\star + \xi} \frac{d\mathcal{F}}{ds} e^{CH_\varepsilon(s - t_\star)} \, ds. \tag{A 6}$$

By assumption, $d\mathcal{F}/ds$ is continuous except at $t = t^\star$ and bounded everywhere. Hence, the bounded convergence theorem allows us to take the limit $\varepsilon \to 0$ inside both integrals, which can both be integrated directly by properties of the Heaviside function $H(s - t_\star)$. Now, taking $\xi \to 0$, we use continuity of $\mathcal{F}$ to show that $\lim_{\xi \to 0} \lim_{\varepsilon \to 0} Q_{\varepsilon,\xi} = 0$. In this same limiting order, we can evaluate the term $[\cdot]_{t_\star - \xi}^{t_\star + \xi}$ in (A 5).

Therefore, in the limit $\varepsilon \to 0$, we combine these results and take $t \to t_\star^+$. This gives $u'(t_\star^+)e^C = u'(t_\star^-) + C^{-1}\mathcal{F}(t_\star, u(t_\star))(e^C - 1)$. Multiplying through by e^{-C} and subtracting $u'(t_\star^-)$ from both sides gives the required jump

$$[u'(t_\star)]_-^+ = (1 - e^{-C}) \left(\frac{1}{C} \mathcal{F}(t_\star, u(t_\star)) - u'(t_\star^-) \right). \tag{A 7}$$

It should be noted that the jump is independent of $\mathcal{G}$ and the choice of φ. In the limit $C \to 0$, we obtain $[u'(t_\star)]_-^+ = \mathcal{F}(t_\star, u(t_\star))$, which is consistent with the original formulation.

Appendix B. The energy of the wave field

We briefly derive the energy perturbation created by the presence of the droplet and associated waves (in dimensional variables). The perturbed surface energy is

$$\Delta \text{SE} = \int_{\mathbb{R}^2} \sigma (\sqrt{1 + |\nabla \eta|^2} - 1) \, dx \, dy \sim \int_{\mathbb{R}^2} \sigma \frac{1}{2} |\nabla \eta|^2 \, dx \, dy \tag{B 1}$$

for small perturbations. By noting that $|\nabla \eta|^2 = \nabla \cdot (\eta \nabla \eta) - \eta \nabla_H^2 \eta$ and that $\eta \to 0$ as $|\boldsymbol{x}| \to \infty$, an application of Green's theorem yields

$$\Delta \text{SE} = \frac{-\sigma}{2} \int_{\mathbb{R}^2} \eta \nabla_H^2 \eta \, dx \, dy. \tag{B 2}$$

For the gravitational potential energy, we introduce variables ζ and $\tilde{\eta}$ to represent z and η in the stationary frame. Specifically, we define $\zeta = z + A \cos(\omega_0 t + \beta)$ and $\tilde{\eta} = \eta + A \cos(\omega_0 t + \beta)$. Without loss of generality, we set the gravitational energy to be zero at $\zeta = 0$. Thus,

$$\begin{aligned} \Delta \text{GPE} &= \int_{\mathbb{R}^2} \int_{-\infty}^{\tilde{\eta}} \rho g \zeta \, d\zeta \, dx \, dy - \int_{\mathbb{R}^2} \int_{-\infty}^{A \cos(\omega_0 t + \beta)} \rho g \zeta \, d\zeta \, dx \, dy \\ &= \int_{\mathbb{R}^2} \int_0^\eta \rho g z \, dz \, dx \, dy. \end{aligned} \tag{B 3}$$

Hence,

$$\Delta \text{GPE} = \frac{1}{2} \rho g \int_{\mathbb{R}^2} \eta^2 \, dx \, dy. \tag{B 4}$$

It should be noted that the velocity potential ϕ is defined in the vibrating frame, and $|\nabla \phi| = \mathbf{0}$ when there are no waves. Hence, by neglecting the energy from the small vortical component near the surface, the kinetic energy perturbation is

$$\Delta \text{KE} = \int_{\mathbb{R}^2} \int_{-\infty}^\eta \frac{1}{2} \rho |\nabla \phi|^2 \, dz \, dx \, dy. \tag{B 5}$$

By the continuity equation (2.1), $|\nabla\phi|^2 = \nabla \cdot (\phi\nabla\phi)$. As $|\nabla\phi| \to \mathbf{0}$ in the far field, we apply the divergence theorem to reduce the problem to the surface integral

$$\Delta\text{KE} = \frac{1}{2}\rho \int_{\mathbb{R}^2} \phi\frac{\partial\phi}{\partial z}\,\mathrm{d}x\,\mathrm{d}y. \tag{B 6}$$

Scaling the wave energy with the typical kinetic energy ($\rho\lambda^5 T^{-2}$), we use (B 2)–(B 6) to define the total energy dimensionless energy perturbation

$$E = \tfrac{1}{2}\langle\phi, \phi_z\rangle + \tfrac{1}{2}G\langle\eta, \eta\rangle - \tfrac{1}{2}B\langle\eta, \nabla_H^2\eta\rangle, \tag{B 7}$$

where we define the inner product

$$\langle f, g\rangle = \int_0^{2\pi}\int_0^\infty rf(r, \theta)g(r, \theta)\,\mathrm{d}r\,\mathrm{d}\theta. \tag{B 8}$$

Using the basis function expansions (3.7)–(3.8) and orthogonality, we can express the first inner product in terms of $a_m(t; k)$, $b_m(t; k)$, and their time derivatives. The second inner product can be simplified via simple orthogonality. The third is easily simplified by recalling that the basis functions Φ and Ψ are orthogonal eigenfunctions of Laplace's equation.

Appendix C. Slow-walking analysis

We now state equations for Γ_2, $a_0^{(2)}$, $a_2^{(2)}$ and $a_1^{(3)}$. The ODE inhomogeneities are

$$\mathcal{H}_0^{(2)} = \Gamma_2\omega_g^2(k)\cos(4\pi t + \beta)a_0^{(0)}(t; k), \tag{C 1}$$

$$\mathcal{H}_2^{(2)} = 0, \tag{C 2}$$

$$\mathcal{H}_1^{(3)} = \Gamma_2\omega_g^2(k)\cos(4\pi t + \beta)a_1^{(1)}(t; k), \tag{C 3}$$

with jump condition inhomogeneities

$$\mathcal{J}_0^{(2)} = \left(\frac{k}{2}\right)^2 P_0(k), \quad \mathcal{J}_2^{(2)} = -\frac{1}{2}\left(\frac{k}{2}\right)^2 P_2(k), \quad \mathcal{J}_1^{(3)} = \frac{1}{2}\left(\frac{k}{2}\right)^3 P_1(k) \tag{C 4a–c}$$

and boundary inhomogeneities

$$\mathcal{B}_0^{(2)} = -\left(\frac{k}{2}\right)^2 a_0^{(0)}(0; k) - \left(\frac{k}{2}\right)a_1^{(1)}(0; k), \tag{C 5}$$

$$\mathcal{B}_2^{(2)} = \left(\frac{k}{2}\right)^2 a_0^{(0)}(0; k) + \left(\frac{k}{2}\right)a_1^{(1)}(0; k), \tag{C 6}$$

$$\mathcal{B}_1^{(3)} = -\left(\frac{k}{2}\right)^3 a_0^{(0)}(0; k) - \frac{3}{2}\left(\frac{k}{2}\right)^2 a_1^{(1)}(0; k) + ka_0^{(2)}(0; k) - \left(\frac{k}{2}\right)a_2^{(2)}(0; k). \tag{C 7}$$

To close the system, (5.9) requires

$$0 = \int_0^\infty \frac{k^2}{2}a_1^{(3)}(0; k)\,\mathrm{d}k. \tag{C 8}$$

REFERENCES

ABRAMOWITZ, M. & STEGUN, I. 1964 *Handbook of Mathematical Functions*. Dover.

BENJAMIN, T. B. & URSELL, F. 1954 The stability of the plane free surface of a liquid in vertical periodic motion. *Proc. R. Soc. Lond.* A **225**, 505–515.

BORGHESI, C., MOUKHTAR, J., LABOUSSE, M., EDDI, A., FORT, E. & COUDER, Y. 2014 Interaction of two walkers: wave-mediated energy and force. *Phys. Rev. E* **90**, 063017.

DE BROGLIE, L. 1926 *Ondes et Mouvements*. Gauthier-Villars.

BUSH, J. W. M. 2015 Pilot-wave hydrodynamics. *Annu. Rev. Fluid Mech.* **47**, 269–292.

BUSH, J. W. M., OZA, A. U. & MOLÁČEK, J. 2014 The wave-induced added mass of walking droplets. *J. Fluid Mech.* **755**, R7.

CATLLÁ, A. J., SCHAEFFER, D. G., WITELSKI, T. P., MONSON, E. E. & LIN, A. L. 2008 On spiking models for synaptic activity and impulsive differential equations. *SIAM Rev.* **50** (3), 553–569.

COUDER, Y. & FORT, E. 2006 Single-particle diffraction and interference at a macroscopic scale. *Phys. Rev. Lett.* **97**, 1541017.

COUDER, Y. & FORT, E. 2011 Probabilities and trajectories in a classical wave–particle duality. *J. Phys.: Conf. Ser.* **361**, 012001.

COUDER, Y., FORT, E., GAUTIER, C.-H. & BOUDAOUD, A. 2005*a* From bouncing to floating: noncoalescence of drops on a fluid bath. *Phys. Rev. Lett.* **94**, 177801.

COUDER, Y., PROTIÈRE, S., FORT, E. & BOUDAOUD, A. 2005*b* Walking and orbiting droplets. *Nature* **437**, 208.

DAMIANO, A. P., BRUN, P.-T., HARRIS, D. M., GALEANO-RIOS, C. A. & BUSH, J. W. M. 2016 Surface topography measurements of the bouncing droplet experiment. *Exp. Fluids* **57** (163), 1–7.

DIAS, F., DYACHENKO, A. I. & ZAKHAROV, V. E. 2008 Theory of weakly damped free-surface flows: a new formulation based on potential flow solutions. *Phys. Lett.* A **372**, 1297–1302.

EDDI, A., FORT, E., MOISY, F. & COUDER, Y. 2009 Unpredictable tunneling of a classical wave–particle association. *Phys. Rev. Lett.* **102**, 240401.

EDDI, A., MOUKHTAR, J., PERRARD, S., FORT, E. & COUDER, Y. 2012 Level splitting at macroscopic scale. *Phys. Rev. Lett.* **108**, 264503.

EDDI, A., SULTAN, E., MOUKHTAR, J., FORT, E., ROSSI, M. & COUDER, Y. 2011 Information stored in Faraday waves: the origin of a path memory. *J. Fluid. Mech.* **674**, 433–463.

EDDI, A., TERWAGNE, D., FORT, E. & COUDER, Y. 2008 Wave propelled ratchets and drifting rafts. *Europhys. Lett.* **82**, 44001.

FILOUX, B., HUBERT, M. & VANDEWALLE, N. 2015 Strings of droplets propelled by coherent waves. *Phys. Rev. E* **92**, 041004(R).

FORT, E., EDDI, A., BOUDAOUD, A., MOUKHTAR, J. & COUDER, Y. 2010 Path-memory induced quantization of classical orbits. *Proc. Natl Acad. Sci. USA* **107** (41), 17515–17520.

GILET, T. & BUSH, J. W. M. 2009 Chaotic bouncing of a droplet on a soap film. *Phys. Rev. Lett.* **102**, 014501.

GILET, T., TERWAGNE, D., VANDEWALLE, N. & DORBOLO, S. 2008 Dynamics of a bouncing droplet onto a vertically vibrated interface. *Phys. Rev. Lett.* **100**, 167802.

HARRIS, D. M. & BUSH, J. W. M. 2014 Droplets walking in a rotating frame: from quantized orbits to multimodal statistics. *J. Fluid Mech.* **739**, 444–464.

HARRIS, D. M., MOUKHTAR, J., FORT, E., COUDER, Y. & BUSH, J. W. M. 2013 Wavelike statistics from pilot-wave dynamics in a circular corral. *Phys. Rev. E* **88**, 011001.

HARTIGAN, J. A. 1975 *Clustering Algorithms*. Wiley.

HARTIGAN, J. A. & WONG, M. A. 1979 A K-means clustering algorithm. *J. R. Stat. Soc. Ser. C Appl. Stat.* **28** (1), 100–108.

HUBERT, M., ROBERT, D., CAPS, H., DORBOLO, S. & VANDEWALLE, N. 2015 Resonant and antiresonant bouncing droplets. *Phys. Rev. E* **91**, 023017.

KODINARIYA, T. M. & MAKWANA, P. R. 2013 Review on determining number of cluster in k-means clustering. *Intl J. Adv. Res. Comput. Sci. Management Studies* **1** (6), 90–95.

KUMAR, K. 1996 Linear theory of Faraday instability in viscous fluids. *Proc. R. Soc. Lond.* A **452**, 1113–1126.

KUMAR, K. & TUCKERMAN, L. S. 1994 Parametric instability of the interface between two fluids. *J. Fluid Mech.* **279**, 49–68.

LABOUSSE, M., OZA, A., PERRARD, S. & BUSH, J. W. M. 2016 Pilot-wave dynamics in a harmonic potential: quantization and stability of circular orbits. *Phys. Rev.* E **93**, 033122.

LABOUSSE, M. & PERRARD, S. 2014 Non-Hamiltonian features of a classical pilot-wave system. *Phys. Rev.* E **90**, 022913.

LABOUSSE, M., PERRARD, S., COUDER, Y. & FORT, E. 2014 Build-up of macroscopic eigenstates in a memory-based constrained system. *New J. Phys.* **16**, 113027.

MILEWSKI, P. A., GALEANO-RIOS, C. A., NACHBIN, A. & BUSH, J. W. M. 2015 Faraday pilot-wave dynamics: modelling and computation. *J. Fluid Mech.* **778**, 361–388.

MOLÁČEK, J. & BUSH, J. W. M. 2013a Drops bouncing on a vibrating bath. *J. Fluid Mech.* **727**, 582–611.

MOLÁČEK, J. & BUSH, J. W. M. 2013b Drops walking on a vibrating bath: towards a hydrodynamic pilot-wave theory. *J. Fluid Mech.* **727**, 612–647.

OZA, A. U., HARRIS, D. M., ROSALES, R. R. & BUSH, J. W. M. 2014a Pilot-wave dynamics in a rotating frame: on the emergence of orbital quantization. *J. Fluid Mech.* **744**, 404–429.

OZA, A. U., ROSALES, R. R. & BUSH, J. W. M. 2013 A trajectory equation for walking droplets: hydrodynamic pilot-wave theory. *J. Fluid Mech.* **737**, 552–570.

OZA, A. U., WIND-WILLASSEN, Ø., HARRIS, D. M., ROSALES, R. R. & BUSH, J. W. M. 2014b Pilot-wave hydrodynamics in a rotating frame: exotic orbits. *Phys. Fluids* **26**, 082101.

PERRARD, S., LABOUSSE, M., FORT, E. & COUDER, Y. 2014a Chaos driven by interfering memory. *Phys. Rev. Lett.* **113**, 104101.

PERRARD, S., LABOUSSE, M., MISKIN, M., FORT, E. & COUDER, Y. 2014b Self-organization into quantized eigenstates of a classical wave-driven particle. *Nature Comm.* **5**, 3219.

PROTIÈRE, S., BOHN, S. & COUDER, Y. 2008 Exotic orbits of two interacting wave sources. *Phys. Rev.* E **78**, 036204.

PROTIÈRE, S., BOUDAOUD, A. & COUDER, Y. 2006 Particle–wave association on a fluid interface. *J. Fluid Mech.* **554**, 85–108.

WALKER, J. 1978 Drops of liquid can be made to float on the liquid. What enables them to do so? *Sci. Am.* **238**, 151–158.

WIND-WILLASSEN, Ø., MOLÁČEK, J., HARRIS, D. M. & BUSH, J. W. M. 2013 Exotic states of bouncing and walking droplets. *Phys. Fluids* **25**, 082002.